Hindawi
Shock and Vibration
Volume 2020, Article ID 8813476, 27 pages
https://doi.org/10.1155/2020/8813476

Research Article

Vibration-Isolation Performance of a Pile Barrier in an Area of Soft Soil in Shanghai

X. F. Ma,[1,2,3] M. Y. Cao,[2] X. Q. Gu,[2,3] B. M. Zhang,[2] Z. H. Yang,[4] and P. F. Guan[4]

[1]*School of Civil Engineering, Kashi University, Kashi 844006, China*
[2]*Department of Geotechnical Engineering, Tongji University, Shanghai 200092, China*
[3]*Key Laboratory of Geotechnical and Underground Engineering of Ministry of Education, Tongji University, Shanghai 200092, China*
[4]*Shanghai Tunnel Engineering & Rail Transit Design and Research Institute, Shanghai 200092, China*

Correspondence should be addressed to X. Q. Gu; guxiaoqiang@tongji.edu.cn

Received 29 August 2020; Revised 16 September 2020; Accepted 22 September 2020; Published 7 October 2020

Academic Editor: Xing Ma

Environmental vibration caused by traffic can affect the normal operation of precision instruments, and vibration-isolation measures should be taken to reduce such negative effects. The engineering background of this paper is a hard-X-ray tunnel under construction in Shanghai, China. First, field vibration measurements are used to study the characteristics of the ground traffic, maglev, subway, and other vibration sources near the tunnel, as well as the laws governing the propagation of vibration waves in the surface and soil layer. The finite-element modelling is then used to establish a two-dimensional numerical model for the field conditions, and the numerical results are compared with the field vibration measurements to validate the applicability of the numerical model for assessing the effects of environmental vibration. Finally, how the parameters of a pile-barrier vibration-isolation system, a vibration-isolation measure used widely for tunnels, influence its performance is studied. The results show the following: with increasing distance from the vibration source, the amplitude of the vibration acceleration decreases gradually, and the high-frequency part of the vibration wave is attenuated rapidly, whereas the low-frequency part is attenuated very little. The vibration-isolation effect of the pile barrier is directly proportional to the elastic modulus of the pile body, the pile length, and the hollow ratio of the pile, and inversely proportional to the stiffness of the filling material. The pile diameter, pile row number, and row spacing have little influence on the vibration-isolation effect. Increasing the pile diameter attenuates the acceleration amplitude somewhat around 10 Hz but has no effect on it around 5 Hz. Overall, the present numerical method is well suited to evaluating environmental vibration problems.

1. Introduction

With high-speed railways being constructed at a growing rate and speeds increasing on existing railways, vibrations due to traffic loads such as rail transit and high-speed trains are having increasing impacts on the surrounding environment. Vibrations due to traffic loads impact greatly the normal lives and work of residents, the structural safety of old buildings, and the production and use of precision instruments and equipment in factories and universities [1–4]. In particular, the effects of such vibrations on some precision instruments and equipment are to produce inaccurate readings, reduce accuracy, shorten service life, and even prevent normal operation. Therefore, vibrations due to traffic loads require urgent solutions as far as precision instruments and equipment are concerned. Examples include (i) the laboratories of the University of Washington Physics and Astronomy Building affected by light rail [5], (ii) medical buildings to be built above existing subways in Atlanta [6], and (iii) the influence of Beijing Metro Line 4 on precision equipment in the Physics Laboratory of Peking University [7]. Failure to treat vibrations due to traffic loads effectively will lead to immeasurable economic and scientific losses; therefore, it is very important to study the laws governing the propagation of vibration waves induced by traffic loads and propose vibration-reduction solutions.

There have been various previous studies of the characteristics of vibration waves induced by traffic loads and the main measures for alleviating the vibration intensity due to such loads [8–15]. Chen et al. [16] studied the response characteristics of train vibration acceleration in seasonal frozen soil near Daqing in China. Through vibration tests on a subway tunnel in Shanghai in China, Wei et al. [17] concluded that traffic loads mainly induce vertical vibrations. Schillemans [18] used a two-dimensional (2D) finite-element (FE) model to study railway vibration response and proposed vibration-reduction measures. Gardien et al. [19] analyzed the laws governing the propagation of subway vibrations in the Netherlands and studied how different model parameters influenced the calculation results. Liao et al. [20] studied the vibration-isolation effect of piles, found it to be related to the stiffness of piles, and concluded that the vibration-isolation effect of soft piles was better than that of hard piles.

Although the aforementioned research led to some meaningful conclusions, the previous studies generally involved only one vibration source and were focused mostly on the vibration responses of buildings above ground; there has been relatively little research on the vibration responses of underground tunnels with multiple vibration sources. Herein, the vibration-isolation performance of a pile barrier in an area of soft soil is studied based on a hard-X-ray free-electron laser facility under construction in Shanghai. The hard-X-ray tunnel is located in Zhangjiang Science City, which is adjacent to a maglev, metro line 16 (viaduct part), the Luoshan Road viaduct, and Luoshan Road. The vibrations in the surrounding environment are complex, and the aforementioned research results do not meet the needs of the project fully. Therefore, it is necessary to study vibration-isolation measures under the conditions of multiple vibration sources in a soft-soil area.

This paper begins with field vibration measurements being used to study the characteristics of the ground traffic, elevated road traffic, maglev, subway, and other vibration sources, as well as the laws governing the propagation of vibration waves in the surface and soil layer. Next, a numerical model of the field measurements is constructed, and its feasibility is assessed. Finally, a dynamic 2D numerical model of the maglev, Luoshan Road viaduct, Luoshan Road, and hard-X-ray tunnel is established to analyze how various parameters of the pile-barrier system influence its vibration-isolation effect.

2. Field Vibration Measurements

2.1. Problem Outline. The hard-X-ray free-electron laser facility is a major Chinese science and technology infrastructure project with the largest investment and longest construction period in China to date. The hard-X-ray tunnel is located in Zhangjiang Science City and has a buried depth of approximately 30 m and an outer diameter of 7 m. The main sources of vibration near the tunnel are a maglev, metro line 16, Luoshan Road viaduct traffic, and Luoshan Road ground traffic. Being sensitive equipment, the hard-X-ray free-electron laser equipment may be affected by environmental vibrations; therefore, it is necessary to study the characteristics of the ground traffic, maglev, subway, and other vibration sources and the laws governing the propagation of traffic vibration waves in the surface and soil layer.

2.2. Layout of Measuring Points and Measurement Instruments. Two groups of field vibration measurements were carried out. The first group is used to study the characteristics of the ground traffic, maglev, subway, and viaduct traffic near the hard-X-ray tunnel. The detailed locations of the measurement points are given in Table 1, and the site layout is shown in Figure 1. In the second group of field tests, the laws governing the propagation of vibration waves on the surface and in the soil layer are studied by monitoring the propagation of vibration waves induced by the maglev in the soil. The detailed locations of the test points are given in Table 2, and the layout of the field tests is shown in Figure 2. The 941 B high-sensitivity acceleration sensor manufactured by the Institute of Engineering Mechanics of the China Earthquake Administration was used in the field vibration measurements. Because the vibrations induced by traffic loads are mainly vertical vibrations [16, 17], this paper focuses on the vertical vibration acceleration due to traffic loads near the hard-X-ray tunnel.

2.3. Analysis of Field Measurement Results

2.3.1. Characteristics of Vibration Sources around Hard-X-Ray Tunnel. In this study, the SeismoSignal software was used to filter and eliminate trend terms from the field vibration measurement data. In the first group of field measurements, the vertical acceleration time histories of the maglev, metro line16 (viaduct part), Luoshan Road viaduct traffic, and Luoshan Road ground traffic were collected, and the frequency-domain information corresponding to the acceleration time histories was obtained by Fourier transform. The results are shown in Figures 3–6, and the comparison of the vibration acceleration data of the different vibration sources is summarized in Table 3. According to the calculation results, the vibration acceleration amplitudes of the maglev and metro line 16 are the largest, followed by that of the Luoshan Road viaduct traffic, with that of the Luoshan Road ground traffic being the smallest. The vibration acceleration amplitudes of the maglev, metro line 16 (viaduct part), and Luoshan Road viaduct traffic are concentrated mainly at medium and high frequencies, whereas that of the Luoshan Road ground traffic is concentrated mainly at low frequency.

2.3.2. Propagation and Attenuation Laws of Vibration Waves in Soil. The second group of field measurements measured the propagation and attenuation of vibration waves generated by the maglev in the soil. The distance between each measuring point and the maglev and the buried depth of each measuring point are given in Table 2, and the obtained acceleration time histories and their corresponding Fourier transform spectra are shown in Figures 7–14. Comparing the

Table 1: Positions of measurement points in the first group of tests.

GI	GI-1	GI-2	GI-3	GI-4
Distance between measuring point and hard-X-ray tunnel (m)	92	221	305	368
Buried depth (m)	0	0	0	0

Note: the measurement points are used to collect the vibration accelerations as follows: ground traffic on Luoshan Road (GI-1); traffic on Luoshan Road viaduct (GI-2); maglev (GI-3); metro line 16 (viaduct part) (GI-4).

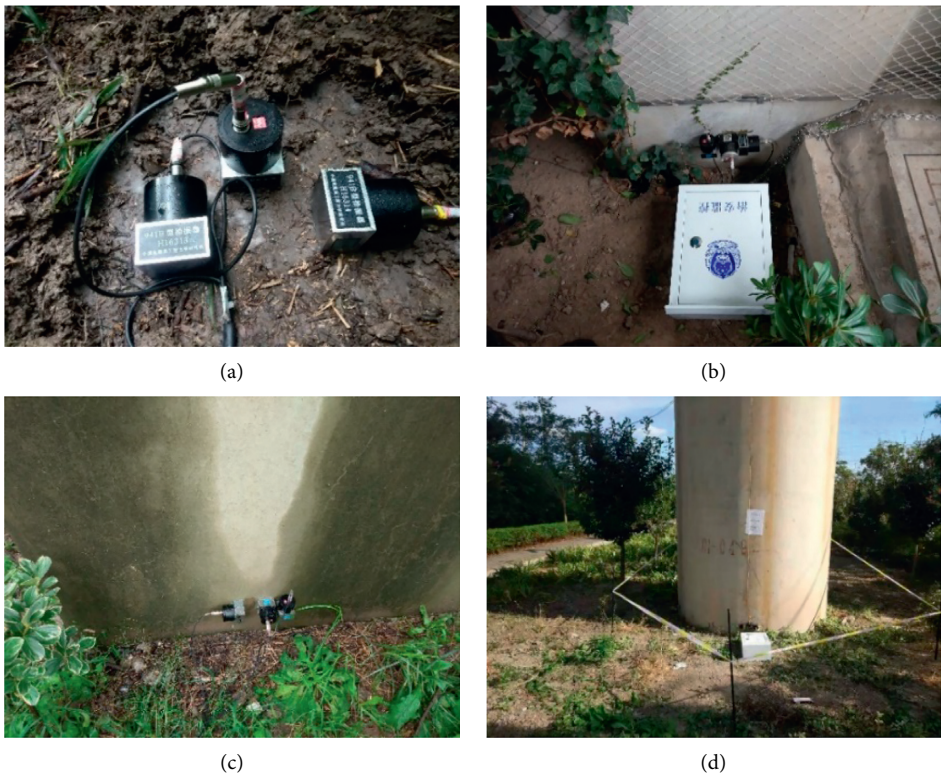

(a) (b) (c) (d)

Figure 1: Layout of measurement points in the first group of field measurements. (a) GI-1. (b) GI-2. (c) GI-3. (d) GI-4.

Table 2: Positions of measurement points in the second group of measurements.

GII	GII-8	GII-7	GII-6	GII-5	GII-4	GII-3	GII-2	GII-1
Distance between measuring point and hard-X-ray tunnel (m)	34	94	160	221	221	221	221	221
Buried depth (m)	0	0	0	0	47.8	34.6	19.1	4.5

vibration time histories and frequency spectra of measurement points GII-5–GII 8 (see Figures 7–10) shows that (i) the amplitude of the vibration acceleration decreased gradually with increasing distance from the vibration source, (ii) the vibration wave was attenuated most obviously in the high-frequency part, and (iii) the attenuation in the low-frequency part was very small. For example, once the vibration wave had travelled 160 m, its part above 40 Hz had largely disappeared and it was basically concentrated below 30 Hz. Comparing the vibration time histories and frequency spectra of measurement points GII-1–GII 5 (see Figures 10–14) shows that the vibration acceleration decreased gradually with increasing depth. For example, once the vibration wave had reached a depth of 47 m, the vibration acceleration amplitude was only 20% of that at the surface.

3. Numerical Analysis

In this part of the study, finite-element (FE) simulation was used to investigate the second group of field measurements. The results of the numerical simulations are compared with the data obtained from the field measurements to verify the effectiveness of the numerical method in simulating environmental vibrations.

3.1. FE Calculation Model. The size of the FE numerical model and the arrangement of the measuring points were established in strict accordance with the actual conditions of the second group of field measurements. The FE model is shown in Figure 15. To meet the required calculation accuracy, the size of the FE model should be 1–1.5 times the

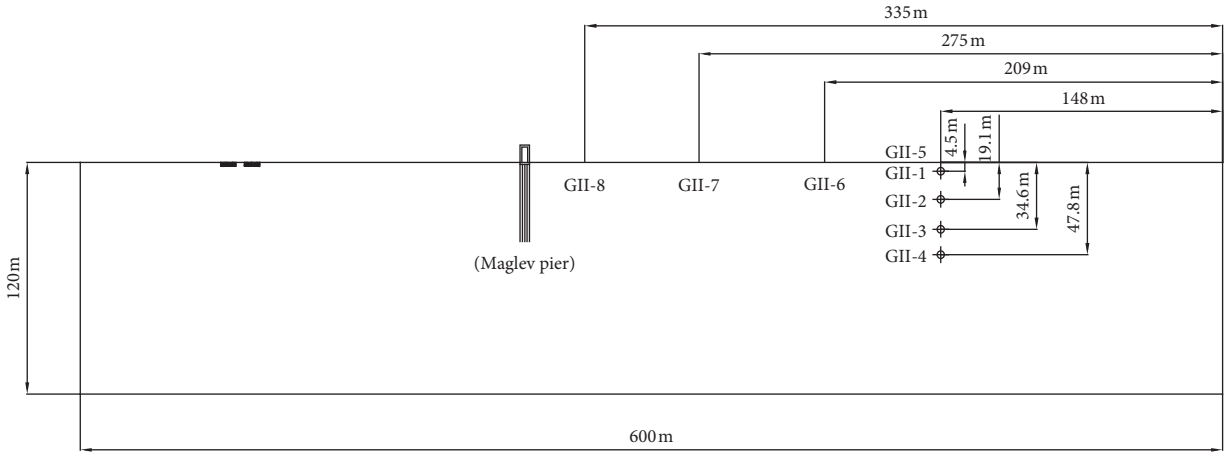

Figure 2: Layout of monitoring points in the second group of field measurements.

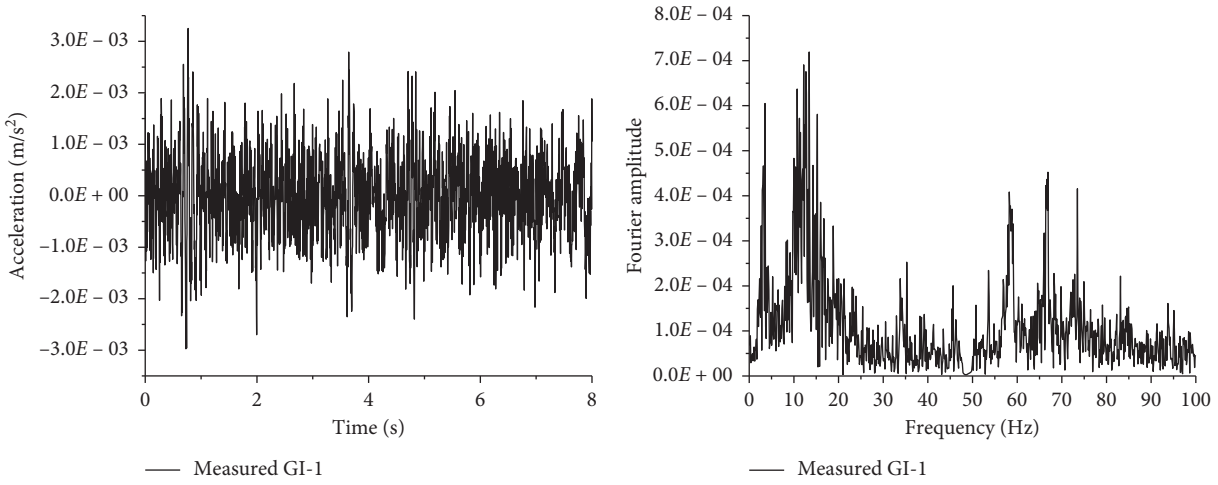

Figure 3: Acceleration: (a) time history and (b) frequency spectrum of GI-1.

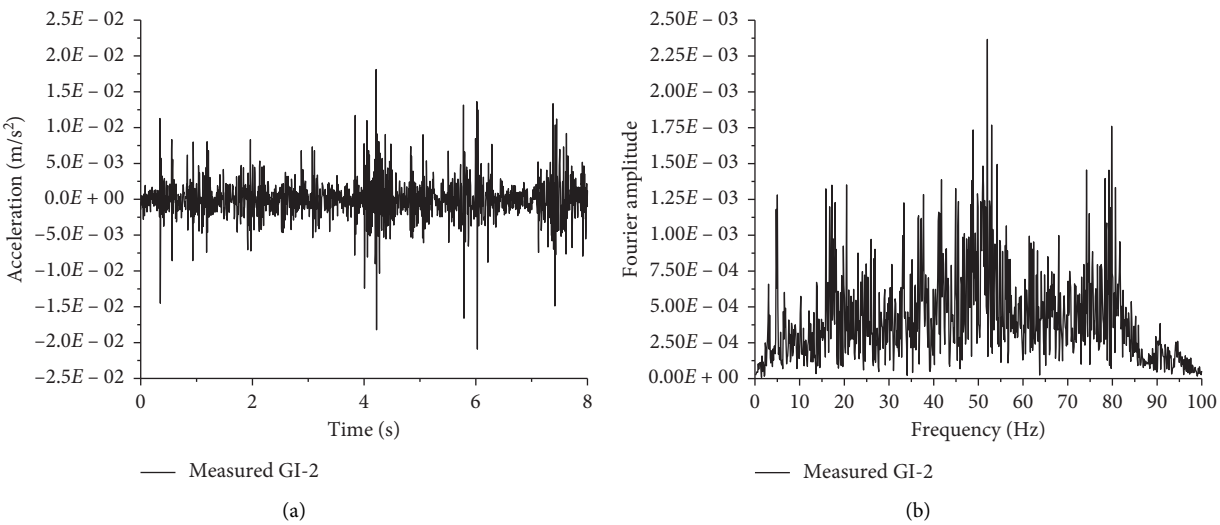

Figure 4: Acceleration: (a) time history and (b) frequency spectrum of GI-2.

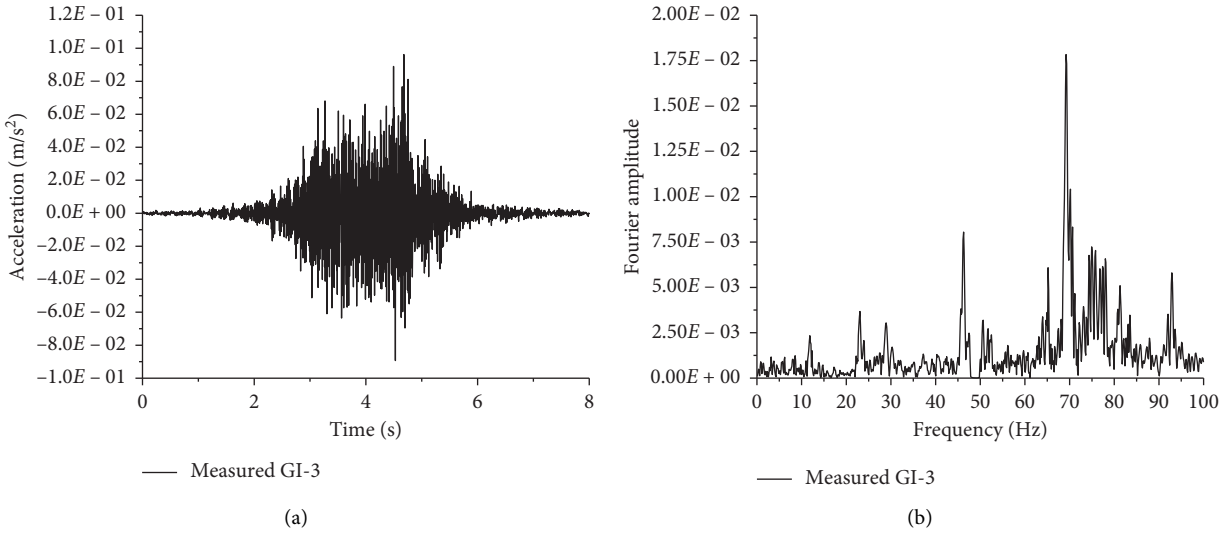

Figure 5: Acceleration: (a) time history and (b) frequency spectrum of GI-3.

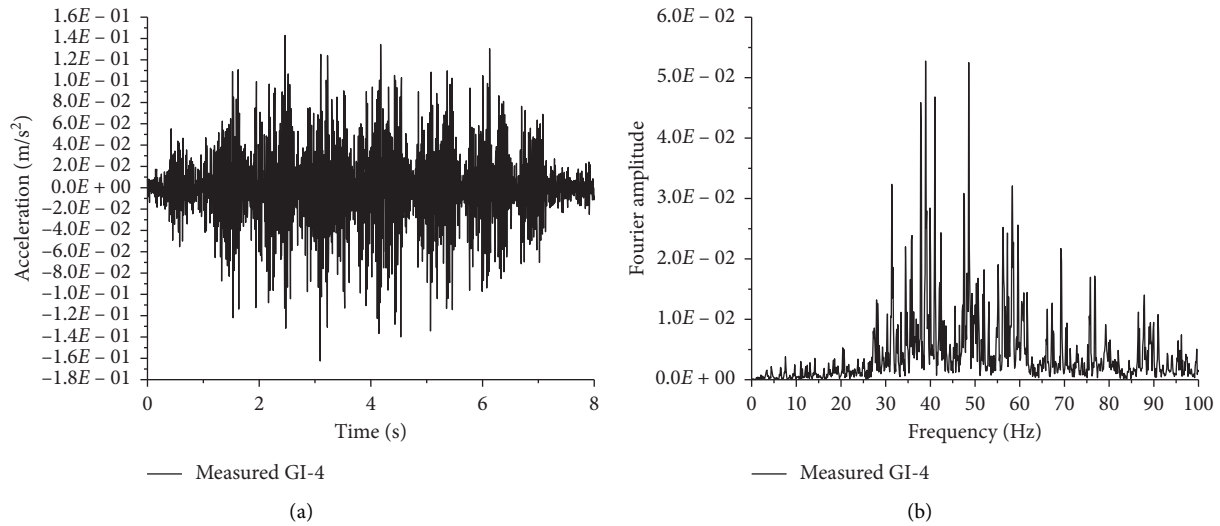

Figure 6: Acceleration: (a) time history and (b) frequency spectrum of GI-4.

Table 3: Comparison of vibration acceleration data of different vibration sources.

Measuring point	Acceleration amplitude (m/s^2)	Frequencies of amplitude (Hz)
GI-1	0.002	10–20, 55–75
GI-2	0.02	20, 52, 80
GI-3	0.14	30–60
GI-4	0.1	70

shear wavelength of interest [21]. According to the field survey data, the maximum wave velocity in the soil layer is 375 m/s (see Table 4), and the field vibration measurements show that the acceleration amplitude is attenuated slowly at 5 Hz (see Figures 7–14), so the shear wavelength of interest is approximately 75 m. Combined with the actual site conditions, the size of the soil FE model was set as 600 m × 120 m.

3.2. Model Material Parameters. For vibrations due to traffic loads, the order of magnitude of the soil strain is generally 10^{-5} or less [22], in which case, the soil is in the elastic state [23] and so the elastic model is adopted in the soil model. The physical and mechanical parameters of the soil are selected according to the field survey data (see Table 4). The in situ shear wave velocities of the soil are measured by suspension logging technique during the site investigation

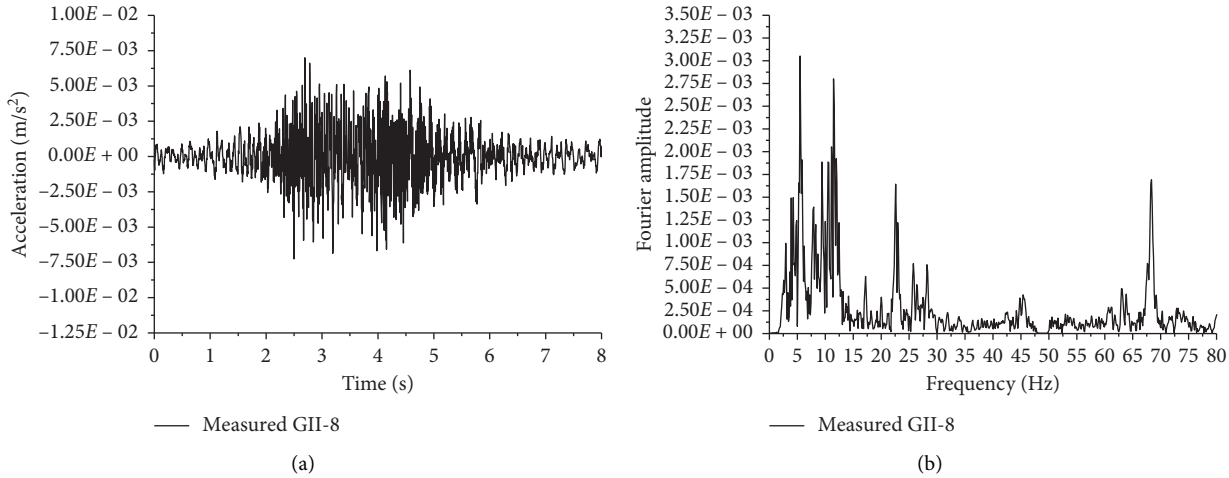

Figure 7: Acceleration: (a) time history and (b) frequency spectrum of GII-8.

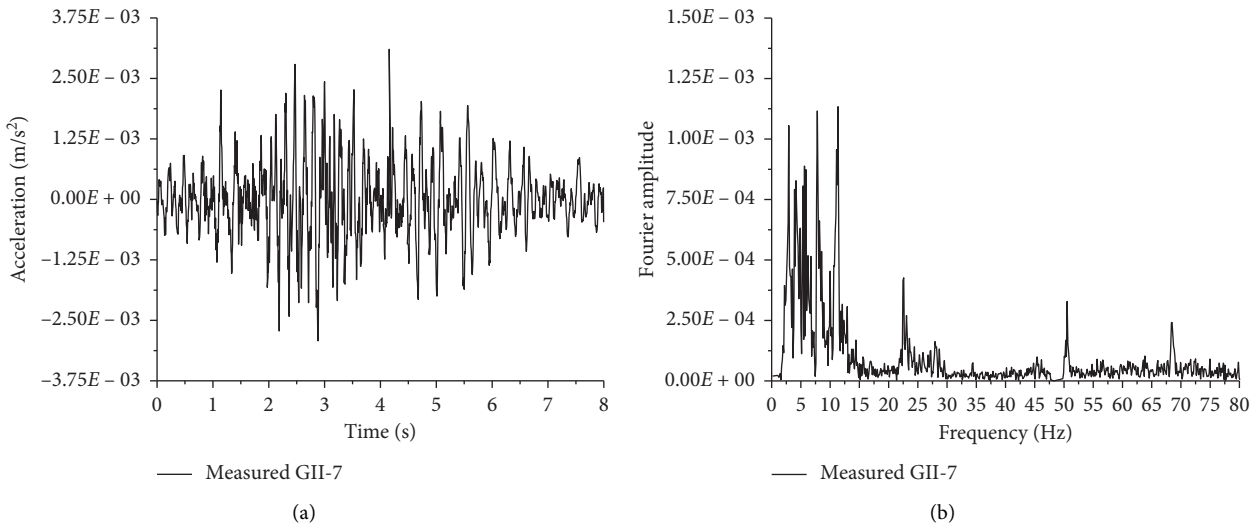

Figure 8: Acceleration: (a) time history and (b) frequency spectrum of GII-7.

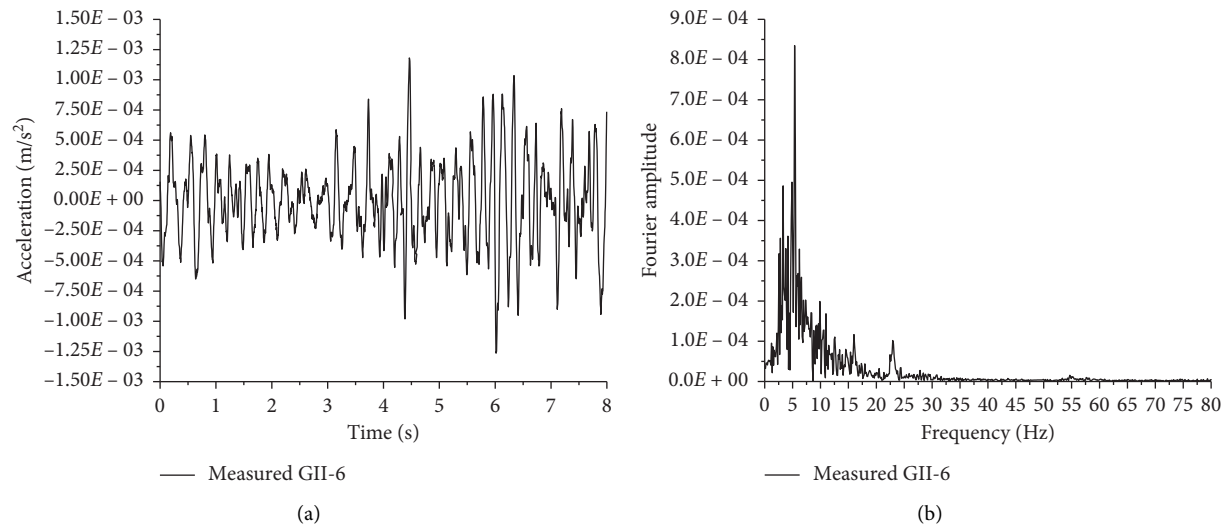

Figure 9: Acceleration: (a) time history and (b) frequency spectrum of GII-6.

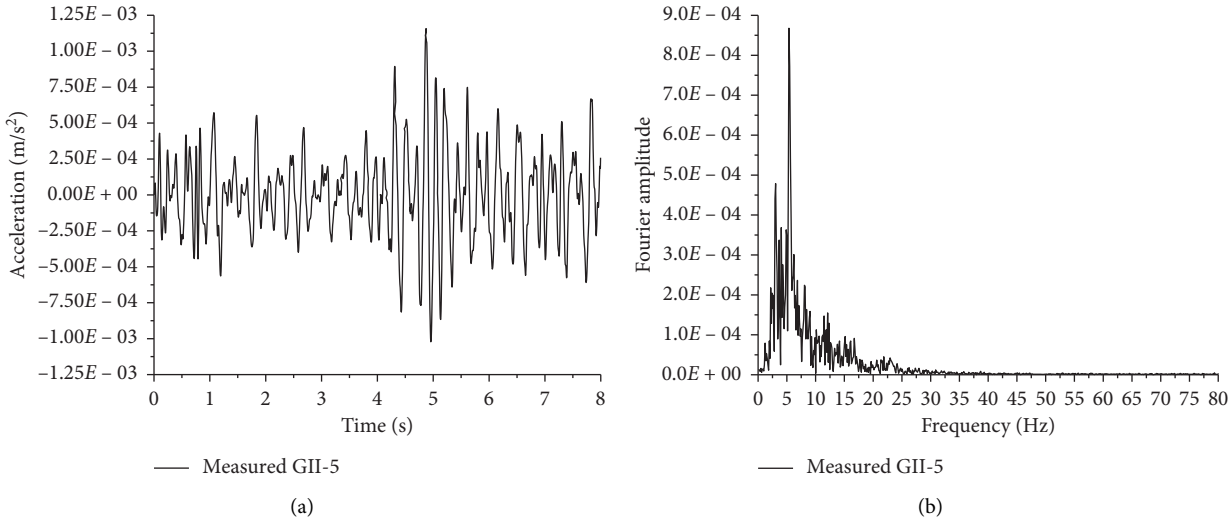

Figure 10: Acceleration: (a) time history and (b) frequency spectrum of GII-5.

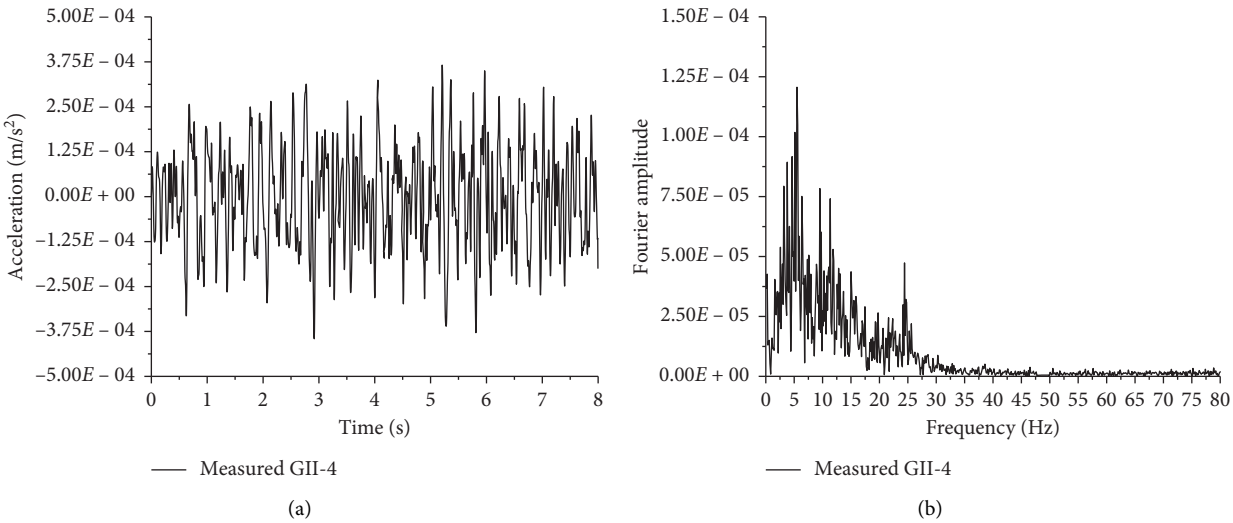

Figure 11: Acceleration: (a) time history and (b) frequency spectrum of GII-4.

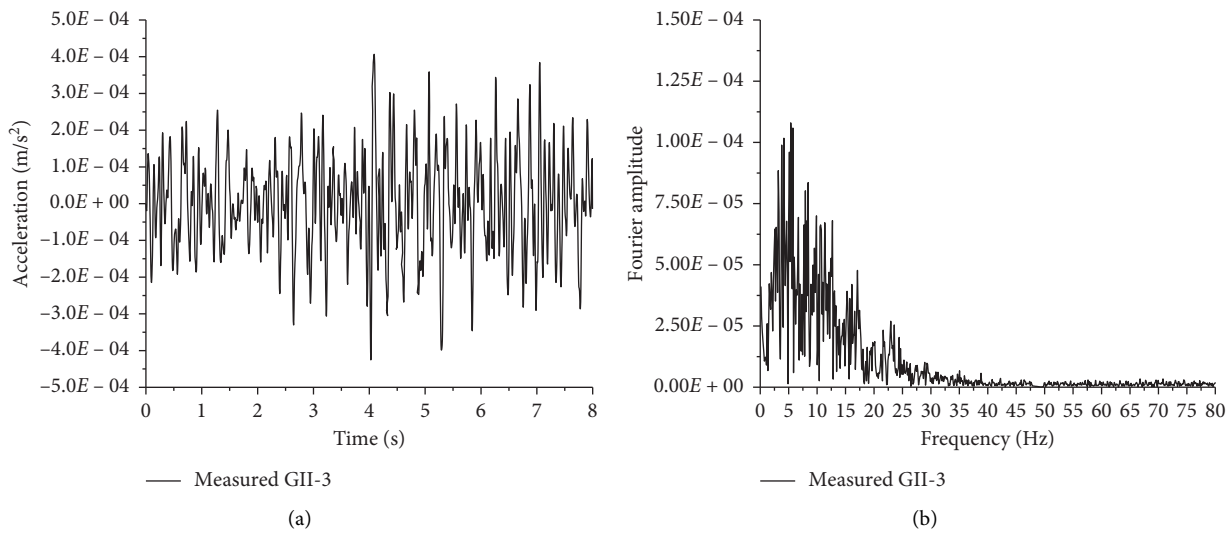

Figure 12: Acceleration: (a) time history and (b) frequency spectrum of GII-3.

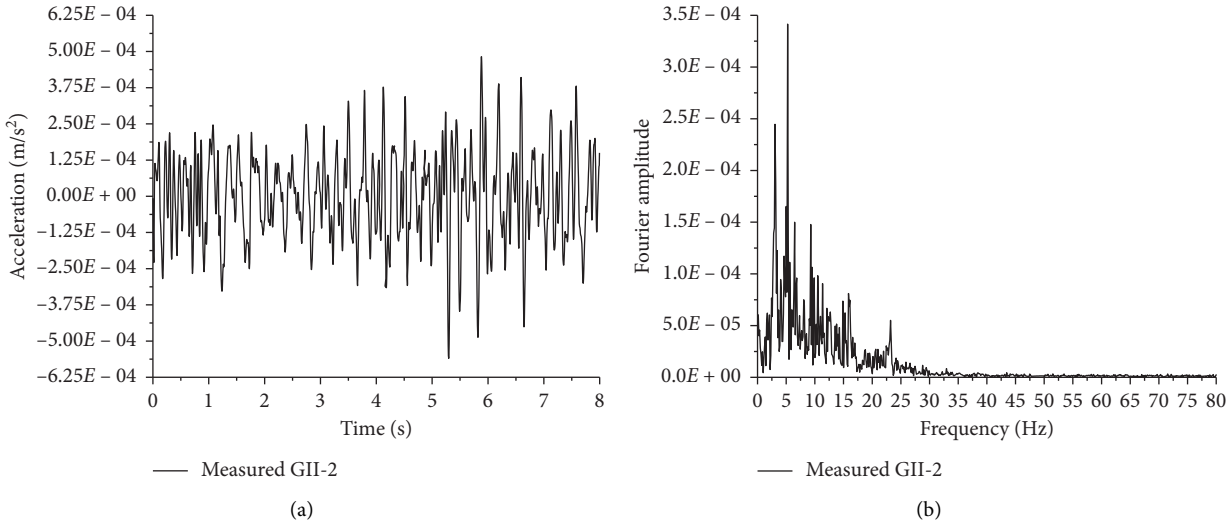

Figure 13: Acceleration: (a) time history and (b) frequency spectrum of GII-2.

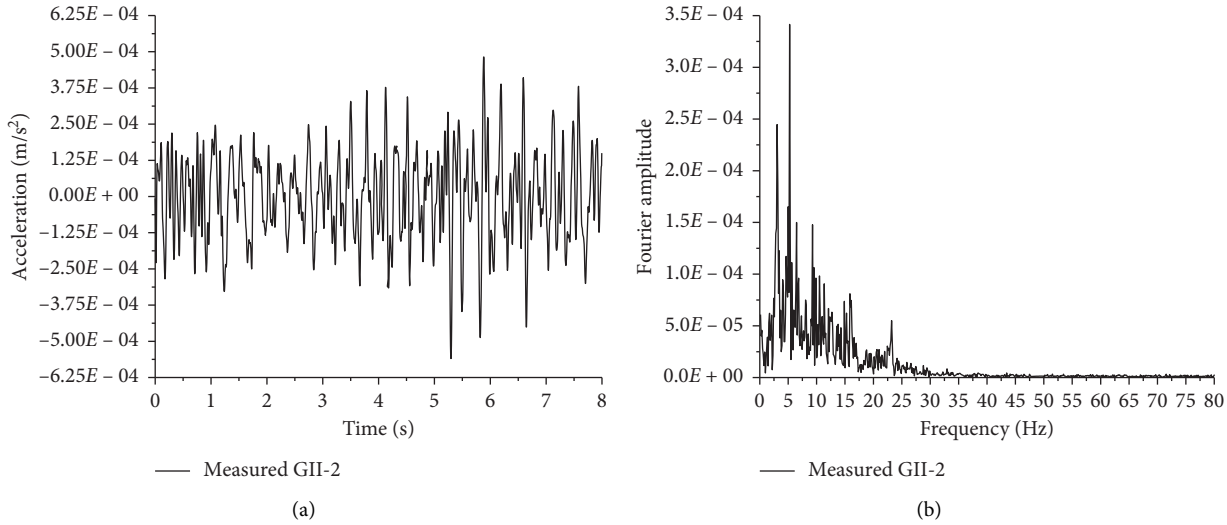

Figure 14: Acceleration: (a) time history and (b) frequency spectrum of GII-1.

and the dynamic shear modulus is calculated as follows [24]:

$$G_d = \rho V_S^2, \tag{1}$$

where G_d is the dynamic shear modulus; V_S is the shear wave velocity of soil; and ρ is the natural density of the soil, which is obtained from the in situ undisturbed soil through laboratory experiments.

The conversion relations between elastic modulus and shear modulus, shear wave velocity, and longitudinal wave velocity are as follows [25]:

$$\begin{aligned} G_d &= \frac{E}{2(1+\nu)}, \\ \frac{V_p}{V_s} &= \sqrt{\frac{2(1+\nu)}{(1-2\nu)}}, \end{aligned} \tag{2}$$

where E is the dynamic elastic modulus; ν is Poisson's ratio; and V_p is the p wave velocity of soil.

The calculation parameters of the maglev viaduct, the pile cap, and the pile foundation are as follows: elastic modulus $E = 30{,}000$ MPa; Poisson's ratio $\nu = 0.176$; density $p = 2500\ \text{kg/m}^3$. In this study, the Rayleigh damping model was used in the 2D dynamic model, and the Rayleigh damping coefficients α and β are given by

$$\begin{cases} \alpha = \dfrac{2\omega_i\omega_j\left(\xi_i\omega_j - \xi_j\omega_i\right)}{\omega_j^2 - \omega_i^2}, \\ \beta = \dfrac{2\left(\xi_j\omega_j - \xi_i\omega_i\right)}{\omega_j^2 - \omega_i^2}, \end{cases} \tag{3}$$

where $\xi_{i,j}$ is the damping ratio corresponding to frequency $\omega_{i,j}$. To obtain the values of α and β, undisturbed soil was

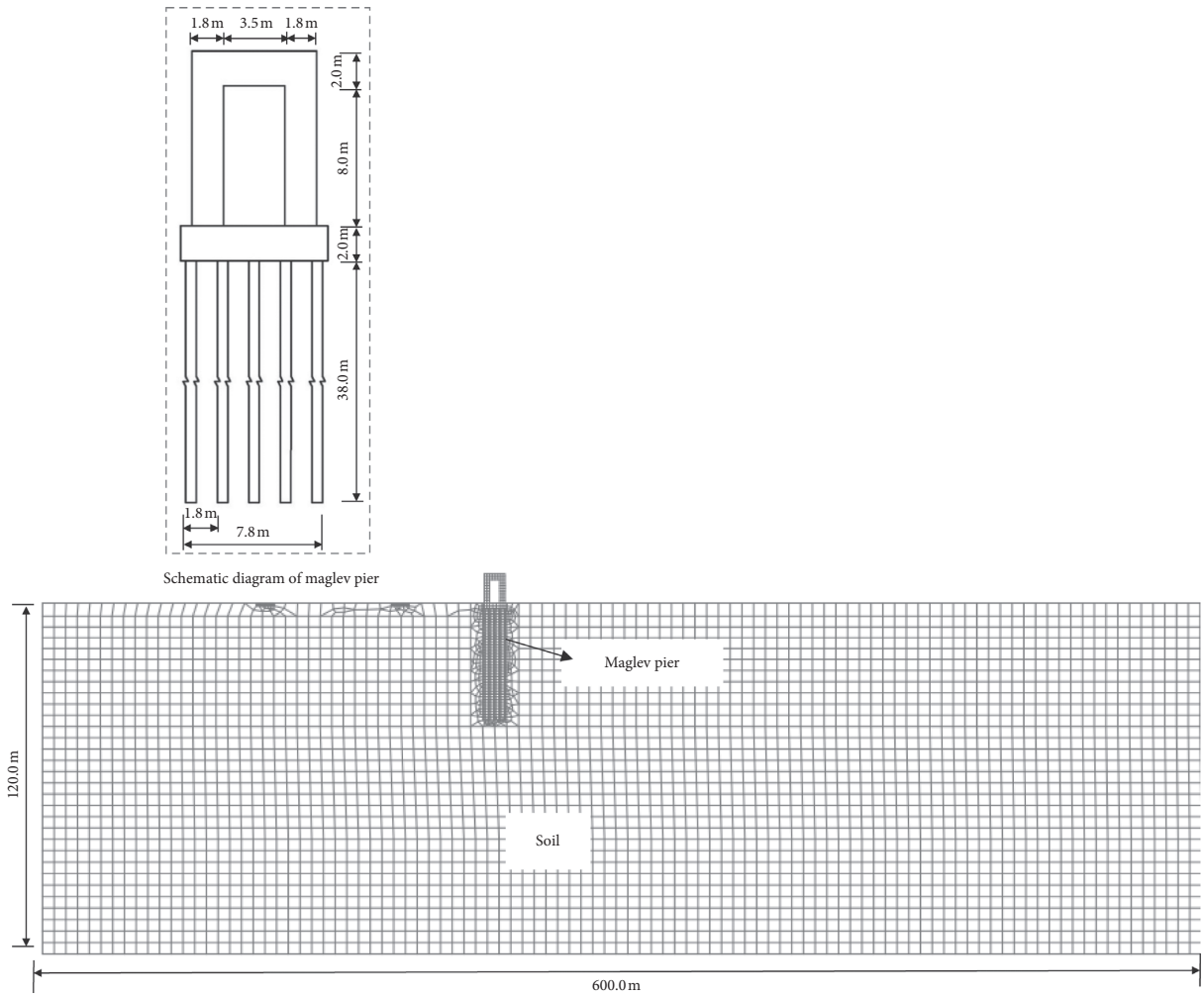

Figure 15: Finite-element (FE) model.

Table 4: Physical and mechanical soil parameters.

Soil	Thickness (m)	Dynamic elastic modulus (MPa)	Dynamic shear modulus (MPa)	Shear wave velocity (m/s)	p wave velocity (m/s)	Poisson's ratio	Density kg·m^{-3})
Silty clay	4.5	85.41	32.11	130.0	363.62	0.33	1900.00
Mucky clay	14.7	94.23	34.90	140.0	420.00	0.35	1780.43
Clayey silt	23	160.83	60.92	180.0	487.44	0.32	1880.20
Fine silty sand 1	38.5	490.46	187.20	300.0	787.73	0.31	2080
Fine silty sand 2	39.3	744.46	295.42	375.0	859.23	0.26	2100.78

subjected to a resonant column test to obtain its damping ratio ξ. The relationship between damping ratio and strain obtained from testing the dynamic characteristics of undisturbed soil is shown in Figure 16, from which it can be seen that when the vibration strain is 10^{-5}, the soil damping ratio is 0.02. Because of the complexity of the damping ratio with frequency, it is assumed that the damping ratio is constant in a certain frequency range of interest. Figure 5 shows that the main vibration frequency band of the maglev is 10–70 Hz, so the $\omega_{i,j}$ values are taken as

$$\begin{cases} \omega_i = 10 \times 2\pi \dfrac{\text{rad}}{\text{s}}, \\ \omega_j = 70 \times 2\pi \dfrac{\text{rad}}{\text{s}}, \\ \xi_i = \xi_j = 0.02. \end{cases} \tag{4}$$

The Rayleigh damping coefficients $\alpha = 2.198$ and $\beta = 7.96 \times 10^{-5}$ are calculated by combining equations (3) and (4). When using the finite-element method to analyze

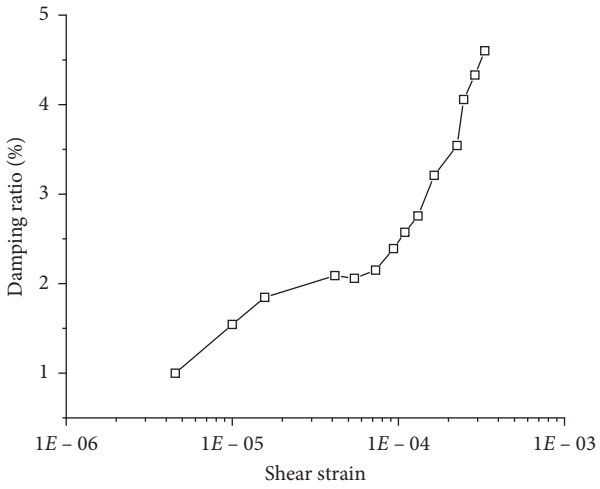

Figure 16: Variation of damping ratio with dynamic shear strain.

the structure-ground dynamic interaction, an artificial boundary usually needs to be applied on the selected calculation area to simulate the radiation damping of the continuous medium, so that the scattered wave does not reflect when passing through the artificial boundary from the inside of the finite calculation area. The artificial boundary of the finite-element model in this paper can be equivalent to a parallel spring-damper system in which the spring stiffness K_B and damping coefficient C_B can be expressed as follows [26]:

Normal boundary:

$$K_{BN} = \alpha_N \frac{G}{R}, \qquad C_{BN} = \rho V_p. \tag{5}$$

Tangential boundary:

$$K_{BT} = \alpha_T \frac{G}{R}, \qquad C_{BT} = \rho V_S, \tag{6}$$

where K_{BN} and K_{BT} are the normal and tangential spring stiffness, respectively; C_{BN} and C_{BT} are the normal and tangential damping coefficients of the damper, respectively; R is the distance from the wave source to the artificial boundary point; and α_N and α_T are artificial boundary parameters. As suggested by Gu [27], the recommended values of α_N and α_T are 1.33 and 0.67, respectively. It should be noted in equations (5) and (6) that the parameter R is expressed by the shortest distance from the vibration source to the artificial boundary. However, in actual problems, the scattering source is not a point source, but line source or area source with spatial distribution. Therefore, the determined spring stiffness in equations (5) and (6) is generally larger.

3.3. Analysis of Results. To verify the correctness of the numerical calculations, the numerical results are compared with the field measurement data in terms of the vibration displacements and the time histories and frequency spectra of the vibration accelerations. These comparisons are shown in Figures 17–25.

Figures 17(a)–24(a) show that the calculated acceleration time histories of GII-7 and GII-8 agree well with the measured field data. However, the calculated acceleration time history of the measuring point far away from the vibration source (e.g., GII-3 and GII-4) is consistent with the measured field data only in the part in which the acceleration amplitude is concentrated; this fact may be related to there being vibration sources other than the maglev in the field measurements.

Figures 17(b)–24(b) show that the calculated acceleration frequency spectrum at each measurement point is basically consistent with the field test data. The calculation results of GII-7 and GII-8 near the vibration source differ considerably from the field measurement data in the low-frequency part; this difference may be related to the fact that R waves are not attenuated on the surface when the latter is acted on by a linear vibration source. The calculated acceleration frequencies of the measuring point far away from the vibration source (e.g., GII-3 and GII-4) are smaller than the field vibration test data; again, this difference may be related to there being vibration sources other than the maglev in the field measurements.

Figure 25(a) shows that the numerically calculated maximum and root mean square (RMS) displacements within 100 m from the vibration source are slightly larger than the field measured data; again, this difference may be related to the fact that R waves are not attenuated on the surface when the latter is acted on by a linear vibration source. However, when the distance from the vibration source exceeds 100 m, the numerically calculated maximum and RMS displacements are close to the field measurement results. Generally speaking, the numerically calculated maximum and RMS displacements of the ground measurement points (GII-5-GII-8) are consistent with the attenuation trend of the field measurement data: with increasing distance from the vibration source, maximum and RMS displacements both decrease gradually.

Figure 25(b) shows that when the depth of the measuring point is less than 35 m, the numerically calculated maximum and RMS displacements are not consistent with the field measured data. However, when that depth exceeds 35 m, the numerically calculated results are relatively close to the field measured data. Generally speaking, the numerically calculated maximum and RMS displacements of the measuring points varying with depth (GII-1-GII-5) are consistent with the field measurement data regarding the attenuation trend: with increasing depth, maximum and RMS displacements both decrease gradually. The numerically calculated results show that the FE numerical method can simulate well the environmental vibration caused by traffic. The subsequent research reported herein analyzes the laws governing the influences of pile material, hollow ratio of the pile, filling material, pile length, pile diameter, and other parameters on the vibration isolation of the pile barrier based on the FE numerical method.

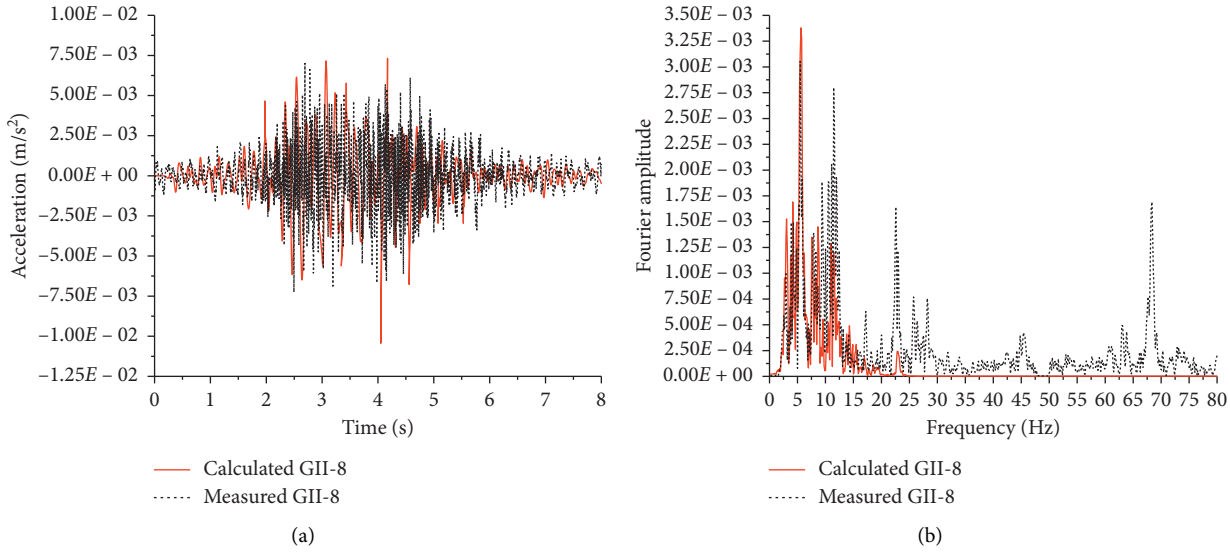

Figure 17: Comparison of numerical and field results (GII-8): (a) acceleration time history; (b) frequency spectrum.

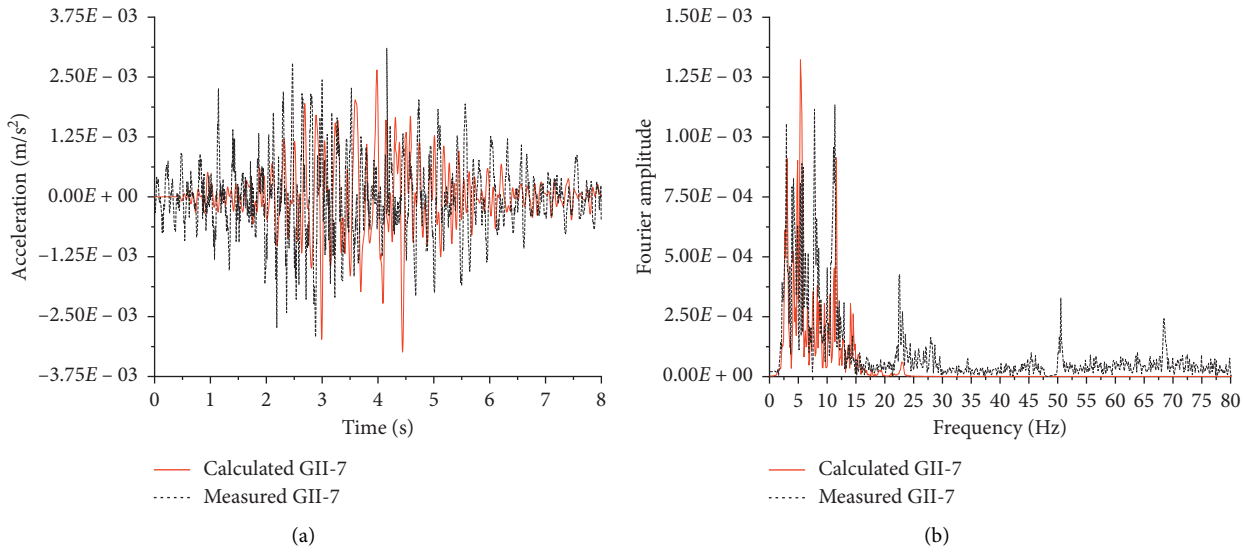

Figure 18: Comparison of numerical and field results (GII-7): (a) acceleration time history; (b) frequency spectrum.

4. Analysis of Vibration-Isolation Performance of Pile Barrier

As a kind of passive isolation barrier system, pile-barrier vibration isolation can eliminate or prevent the adverse effects caused by vibration [28, 29]. This section reports on an extensive numerical parametric investigation of a pile-barrier vibration-isolation system with various pile materials, hollow ratio of the pile, filling materials, pile lengths, pile diameters, vibration-isolation positions, pile spacing, and row numbers to study how each parameter influences the vibration isolation of the pile barrier.

4.1. FE Calculation Model. A 2D model of the maglev, Luoshan Road viaduct, Luoshan Road, and hard-X-ray tunnel was established to study how the pile parameters influence the vibration-isolation effect. The FE model is shown in Figure 26. The outer diameter of the hard-X-ray tunnel model is 7 m, the inner diameter is 6.3 m, and the buried depth is 30 m. The inner and outer rings in the tunnel model are set as a lining layer and a grouting layer, respectively, and the monitoring point is located in the middle of the tunnel floor (see Figure 26). The calculation parameters of the structural model are given in Table 5. See Section 3 for the settings of the soil calculation parameters and FE model, which are not repeated here. The measured acceleration time-history data for the Luoshan Road traffic, Luoshan Road viaduct traffic, and maglev are filtered and used as the load for the numerical calculations, as shown in Figure 27. The calculations were performed first with no pile-barrier vibration-isolation measures in place, after

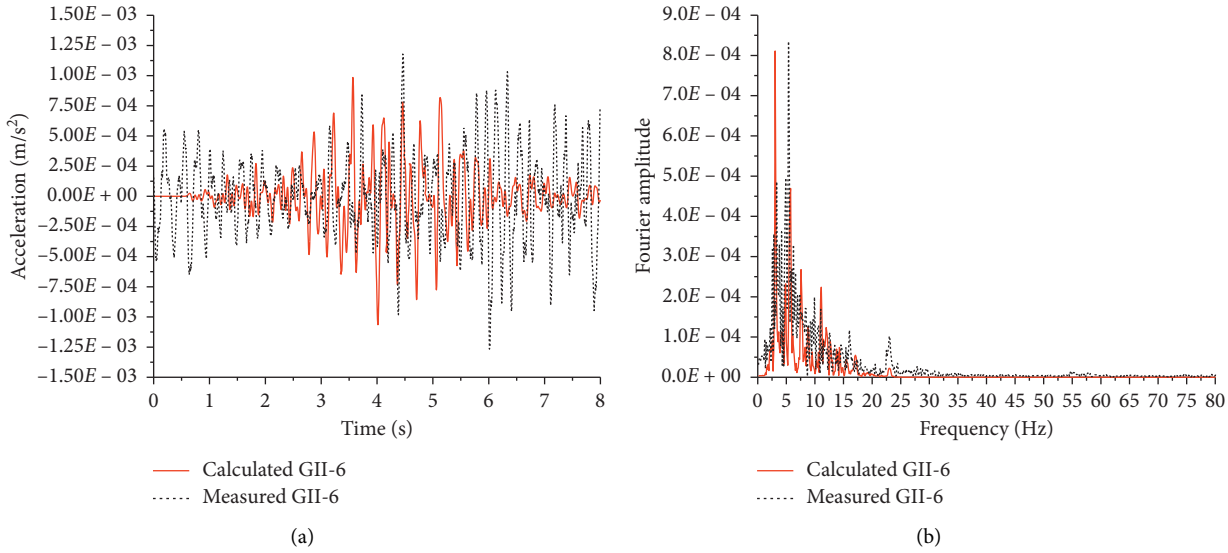

Figure 19: Comparison of numerical and field results (GII-6): (a) acceleration time history; (b) frequency spectrum.

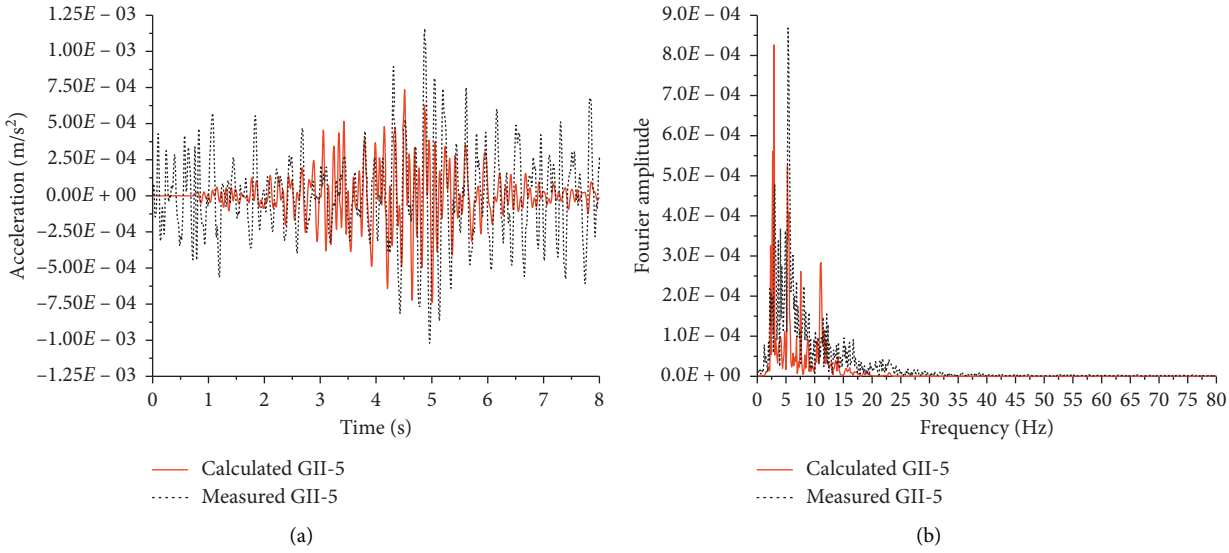

Figure 20: Comparison of numerical and field results (GII-5): (a) acceleration time history; (b) frequency spectrum.

which an extended numerical parametric analysis was performed to study how different pile materials, hollow ratio of the pile, filling materials, pile lengths, pile diameters, pile row numbers, and row spacing affect the vibration isolation of the pile barrier. Details of the parametric analysis are given in Table 6.

4.2. Calculation Results with No Pile Barrier Vibration Isolation. Figure 28 shows the vibration acceleration and displacement time histories and the acceleration frequency spectrum of the tunnel-floor monitoring point obtained from the numerical calculations with no vibration-isolation measures. The numerical calculations show that the maximum and RMS vibration displacements are 1086.64 and 280.95 nm, respectively. The frequency spectrum (see Figure 28(b)) shows that the vibration amplitude is concentrated mainly in the low-frequency part when it propagates to the bottom of the tunnel. Therefore, an effective way to reduce the tunnel vibration displacement is to block the vibration wave effectively in the low-frequency band.

4.3. Influence of Pile Material on Vibration Isolation Effect. In the FE simulation, concrete piles of different strength are set to study how the pile material influences the vibration-isolation performance of the pile barrier. The parameter selection of different pile materials and the calculated maximum and RMS vibration displacements of the monitoring point are shown in Group I of Table 6, and the

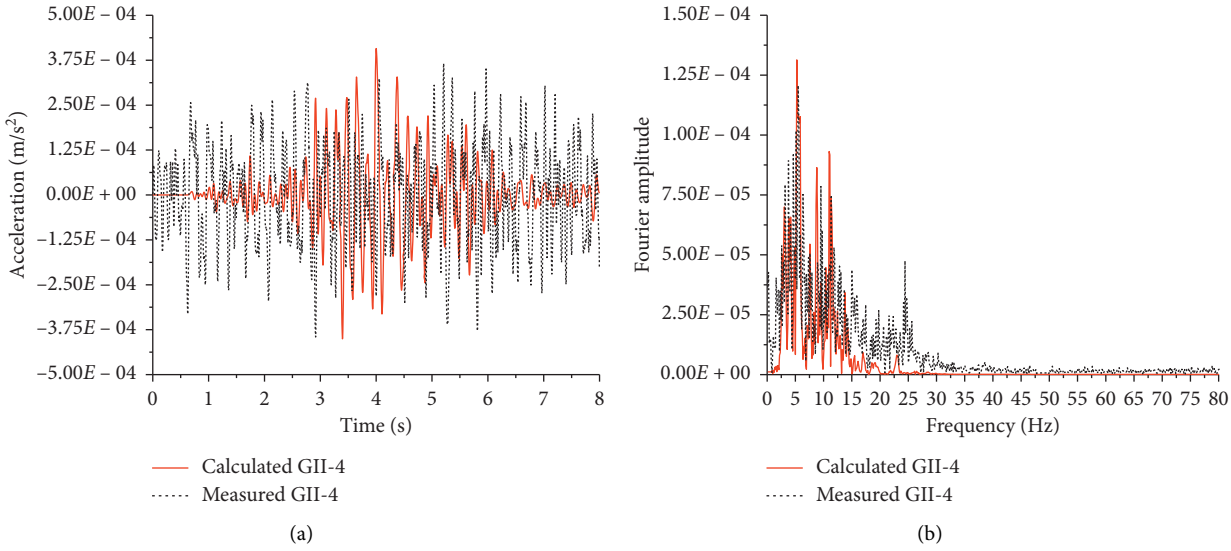

Figure 21: Comparison of numerical and field results (GII-4): (a) acceleration time history; (b) frequency spectrum.

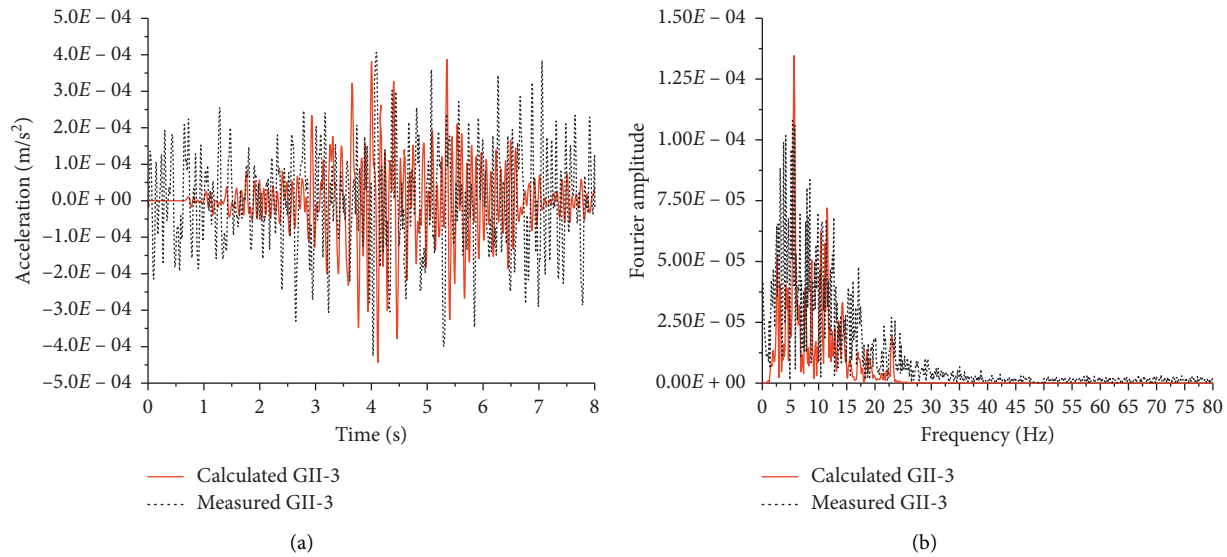

Figure 22: Comparison of numerical and field results (GII-3): (a) acceleration time history; (b) frequency spectrum.

frequency-spectrum comparison for different pile body materials and without vibration-isolation measures is shown in Figure 29. The calculation results show that the vibration-isolation effect is better with increasing pile stiffness when the other conditions remain unchanged. They also show that the vibration-isolation effect of foam plastic and foam concrete with a small elastic modulus is much poorer than that of concrete with a large elastic modulus, but the vibration-isolation effects of concrete piles of different strengths are mostly the same. The vibration-isolation measures adopted in engineering must consider comprehensively the vibration-isolation effect and cost. Therefore, if there is no strength requirement for the piles used for vibration isolation, it is recommended to choose row piles with C20 concrete.

4.4. Influence of Hollow Ratio (r) and Filling Material on Vibration Isolation Effect. Groups II and III of Table 6 investigate how the hollow ratio (r) of the pile and filling material influence the vibration-isolation effect. The calculated maximum and RMS vibration displacements of the monitoring points are shown in the same groups. The frequency-spectrum comparisons between different hollow ratios and filling materials and without vibration-isolation measures are shown in Figures 30 and 31, respectively. The calculation results show that with increasing hollow ratio of the pile, the vibration-isolation capacity improves. For example, the calculated maximum and RMS vibration displacements of piles with a hollow ratio of 0.39 are 48.96% and 34.36%, respectively, of those of solid piles. The calculation results also show that with increasing elastic

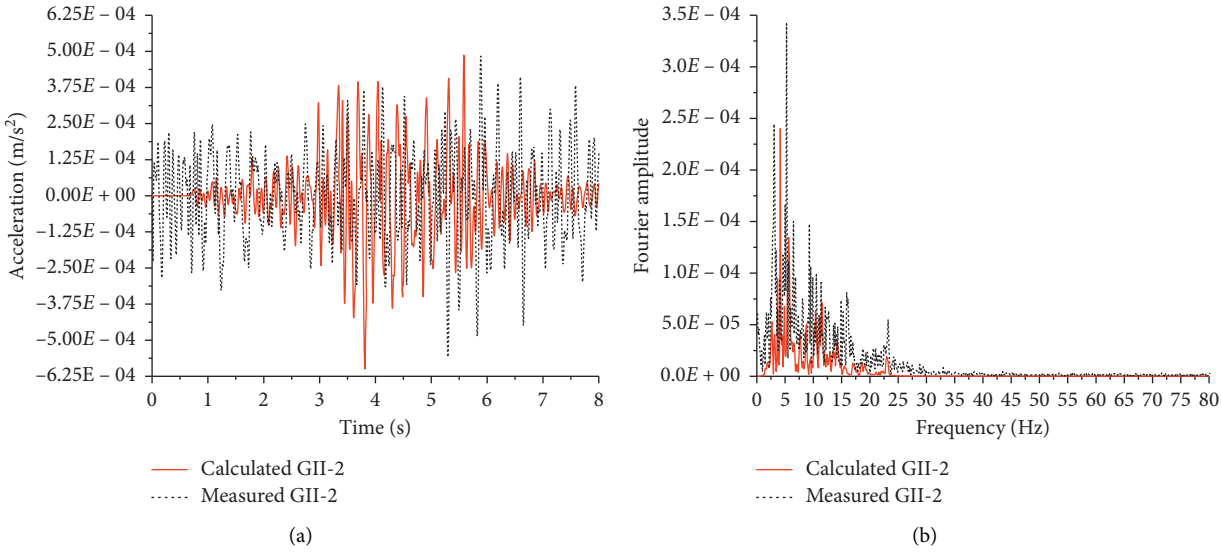

Figure 23: Comparison of numerical and field results (GII-2): (a) acceleration time history; (b) frequency spectrum.

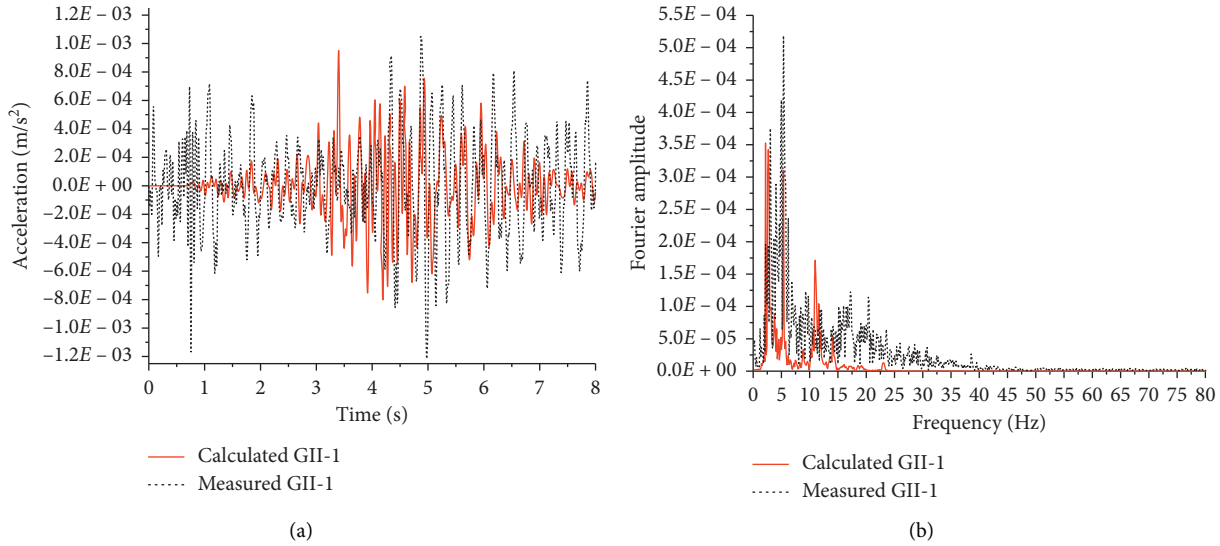

Figure 24: Comparison of numerical and field results (GII-1): (a) acceleration time history; (b) frequency spectrum.

modulus of the filler in the piles, the vibration-isolation capacity decreases gradually.

4.5. Influence of Pile Length (L) and Pile Diameter (D) on Vibration Isolation Effect. Groups IV and V of Table 6 explore the effects of the pile length and diameter. The calculated maximum and RMS vibration displacements of the monitoring points are shown in the same groups. The frequency-spectrum comparison between different pile lengths and diameters and without vibration-isolation measures is shown in Figures 32 and 33, respectively. The calculation results show that the vibration-isolation capacity of the pile barrier increases with increasing pile length. For example, when the pile length is increased from 10 m to 40 m, the maximum and RMS vibration displacements are reduced by 11% and 15.7%, respectively. The calculation results also show that the pile diameter has little influence on the vibration-isolation effect of the piles. Figure 33 shows that increasing the pile diameter has little effect on the acceleration amplitude around 5 Hz but affects it somewhat around 10 Hz.

4.6. Influence of Distance from Hard-X-Ray Tunnel (d) on Vibration Isolation Effect. Group VI of Table 6 shows the effect of the distance from the hard-X-ray tunnel. The calculated maximum and RMS vibration displacements of the monitoring points are shown in the same group. The frequency-spectrum comparison between different distances from the hard-X-ray tunnel and without vibration-isolation measures is shown in Figure 34. According to the calculation

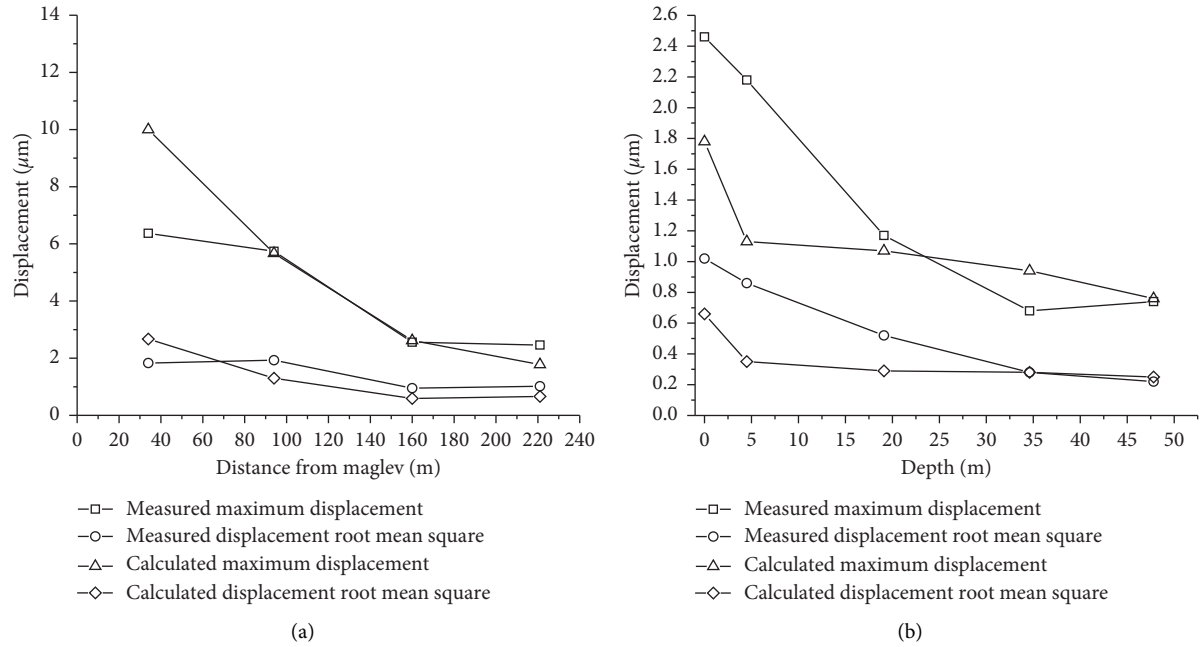

Figure 25: Comparison of numerical and field results: relationships between vibration displacement and (a) distance of surface measuring points from maglev (GII-5–GII-8) and (b) the measuring points varying with depth (GII-1-GII-5).

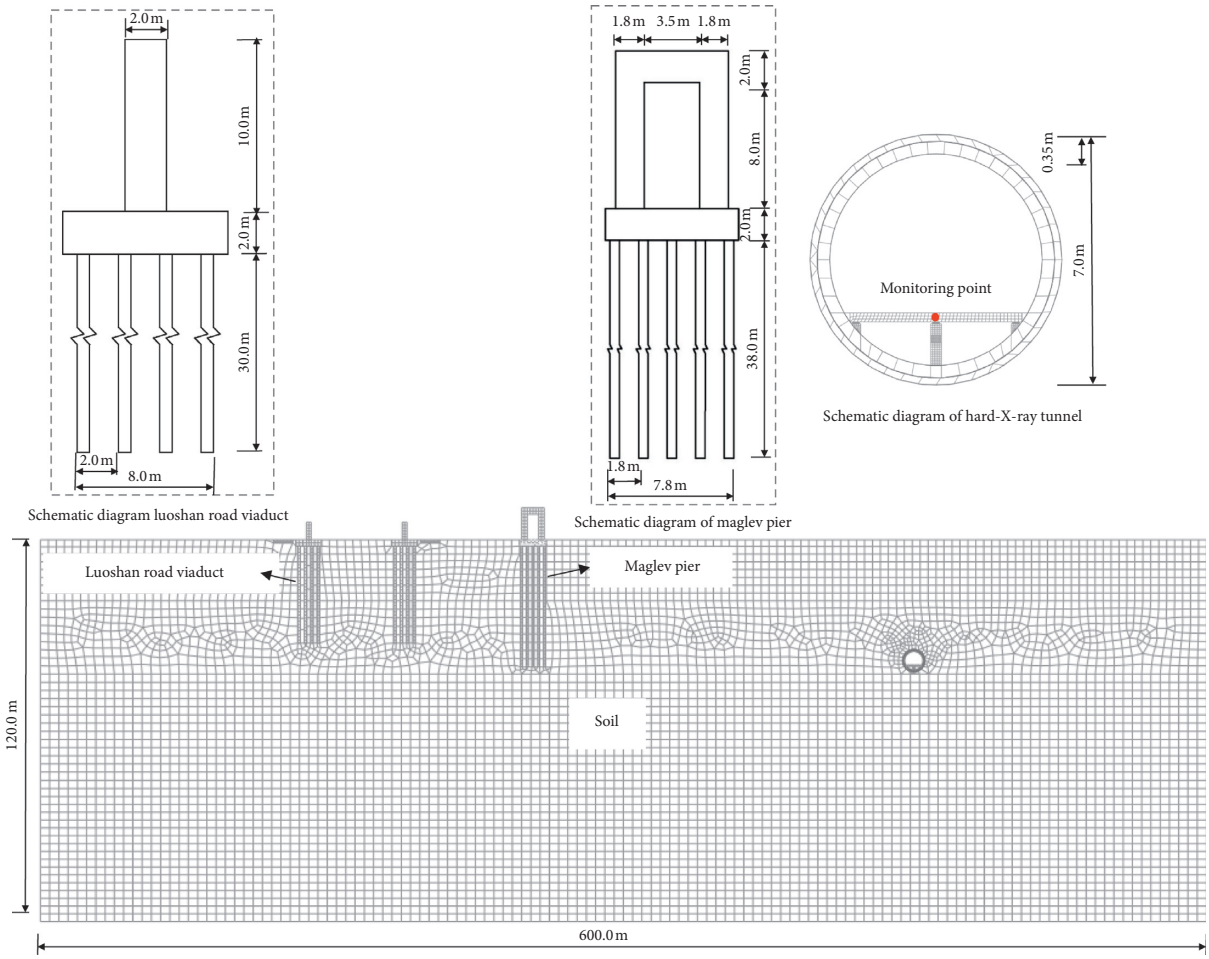

Figure 26: FE model.

Table 5: Calculation parameters of the structural model.

Structure	Elastic modulus (MPa)	Poisson's ratio	Density (kg/m^3)
Pier, pile cap, pile	30,000	0.176	2500
Tunnel grouting layer	30	0.2	2600
Tunnel lining layer	34,500	0.2	2500
Subgrade	1500	0.3	1200

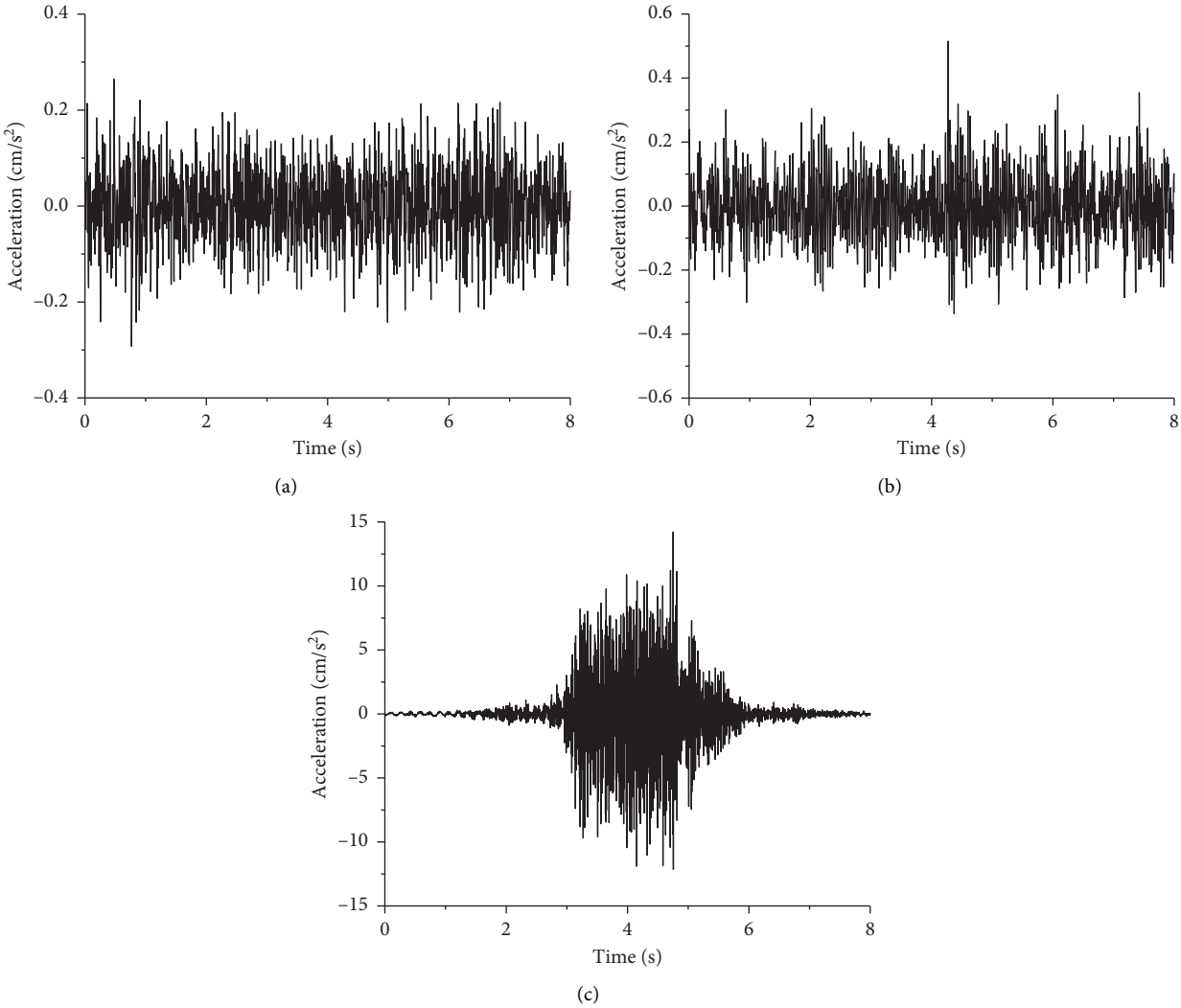

Figure 27: Acceleration time-history curves of vibration source: (a) Luoshan Road traffic, (b) Luoshan Road viaduct traffic, and (c) maglev.

results, the vibration-isolation effect of the piles is no better if the piles are closer to the tunnel. Therefore, the vibration-isolation position of the pile barrier in practical engineering should be considered according to the actual working conditions.

4.7. Influence of Pile Row Number (n) and Row Spacing (c) on Vibration Isolation Effect. Groups VII and VIII of Table 6 evaluate the influences of pile row number and row spacing. The frequency-spectrum comparisons between different pile row numbers and row spacing and without vibration-isolation measures are shown in Figures 35 and 36, respectively. The calculation results show that the vibration-isolation ability of the pile barrier improves gradually with increasing pile row number and decreasing row spacing, but generally speaking, the influences of pile row number and row spacing on the vibration-isolation effect are small.

Table 6: Summary of parametric investigation.

Group	Variable			Other key parameters/configuration	Maximum displacement (nm)	RMS displacement (nm)	Note
I	Pile body material	Foam plastics	ρ (kg/m^3) 700 E (MPa) 2000 ν 0.38	$D = 0.8$ actm; $D_0 = 0.8$ m; $L = 45$ m; $n = 1$; $d = 20$ m	950.41	208.59	Effect of pile body material
		C20 concrete	P (kg/m^3) 2500 E (MPa) 26,000 ν 0.2		865.29	191.57	
		C30 concrete	P (kg/m^3) 2500 E (MPa) 30,000 ν 0.2		825.02	190.27	
		C40 concrete	P (kg/m^3) 2500 E (MPa) 33,000 ν 0.2		827.58	190.28	
		C50 concrete	P (kg/m^3) 2500 E (MPa) 35,000 ν 0.2		828.87	190.29	
		Foam concrete	P (kg/m^3) 800 E (MPa) 400 ν 0.21		942.4	207.53	
II	Hollow ratio (r)	0	D (m) 0.8 D_0 (m) 0.8	$\rho = 2500$ kg/m; $E = 26{,}000$ MPa; $\nu = 0.2$; $L = 45$ m; $n = 1$; $d = 20$ m	865.29	191.57	Effect of hollow ratio, r
		0.39	D (m) 0.8 D_0 (m) 0.65		441.62	125.75	
		0.25	D (m) 0.8 D_0 (m) 0.6		506.84	133.37	
		0.19	D (m) 0.8 D_0 (m) 0.575		505.48	133.43	
		0.14	D (m) 0.8 D_0 (m) 0.55		511.35	134.12	
		0.06	D (m) 0.8 D_0 (m) 0.5		511.28	135.13	
III	Filling material	Loose field soil	ρ_0 (kg/m^3) 1000 E_0 (MPa) 50 ν_0 0.3	$D = 0.8$ m; $D_0 = 0.65$ m; $\rho = 2500$ kg/m; $E = 26{,}000$ MPa; $\nu = 0.2$; $L = 45$ m; $n = 1$; $d = 20$ m	765.61	159.64	Effect of filling material
		Dense field soil	ρ_0 (kg/m^3) 1900 E_0 (MPa) 100 ν_0 0.3		785.67	159.64	
		Foam	ρ_0 (kg/m^3) 45 E_0 (MPa) 2.94 ν_0 0.3		565.77	134.29	
		Cement-soil	ρ_0 (kg/m^3) 1850 E_0 (MPa) 1000 ν_0 0.2		826.16	164.11	
IV	Pile length, L (m)		10	$D = 0.8$ m; $D_0 = 0.8$ m; $\rho = 2500$ kg/m; $E = 26{,}000$ MPa; $\nu = 0.2$; $n = 1$; $d = 20$ m	979.58	227.42	Effect of pile length, L
			20		938.49	219.07	
			30		918.67	217.26	
			40		872.22	191.74	
			50		836.84	187.94	
			60		836.84	186.92	
V	Pile diameter, D (m)		0.3	$D_0 = 0.8$ m; $\rho = 2500$ kg/m; $E = 26{,}000$ MPa; $\nu = 0.2$; $n = 1$; $d = 20$ m	881.9	195.8z	Effect of pile diameter, D
			0.4		879.35	195.03	
			0.5		873.6	192.9	
			0.6		870.36	192.35	
			0.7		867.26	192.02	
			0.8		865.29	191.57	

Table 6: Continued.

Group	Variable		Other key parameters/configuration	Maximum displacement (nm)	RMS displacement (nm)	Note
VI	Distance from hard-X-ray tunnel, d (m)	5	$D = 0.8$ m; $D_0 = 0.8$ m; $\rho = 2500$ kg/m; $E = 26{,}000$ MPa; $\nu = 0.2$; $L = 45$ m; $n = 1$	850.06	182.34	Effect of the distance from hard-X-ray tunnel, d
		10		828.88	180.69	
		20		865.29	191.57	
		30		843.43	191.83	
		40		742.48	177.78	
		50		734.31	167.26	
		60		862.36	185.32	
VII	Pile row number, n	1	$D = 0.8$ m; $D_0 = 0.8$ m; $\rho = 2500$ kg/m; $E = 26{,}000$ MPa; $\nu = 0.2$; $L = 45$ m; $C = 2.5$	865.29	191.57	Effect of pile row number, n
		2		829.73	189.2	
		3		823.27	186.3	
		4		787.53	184.36	
VIII	Row spacing, c (m)	2	$D = 0.8$ m; $D_0 = 0.8$ m; $\rho = 2500$ kg/m; $E = 26{,}000$ MPa; $\nu = 0.2$; $L = 45$ m; $n = 2$	827.36	187.69	Effect of row spacing, c
		2.5		829.73	189.2	
		3		843.26	191.62	
		4		849.73	192.96	
		5		878.36	193.42	
		6		891.68	195.92	

Note: D and D_0 are the outer diameter and inner diameter of the tunnel, respectively.

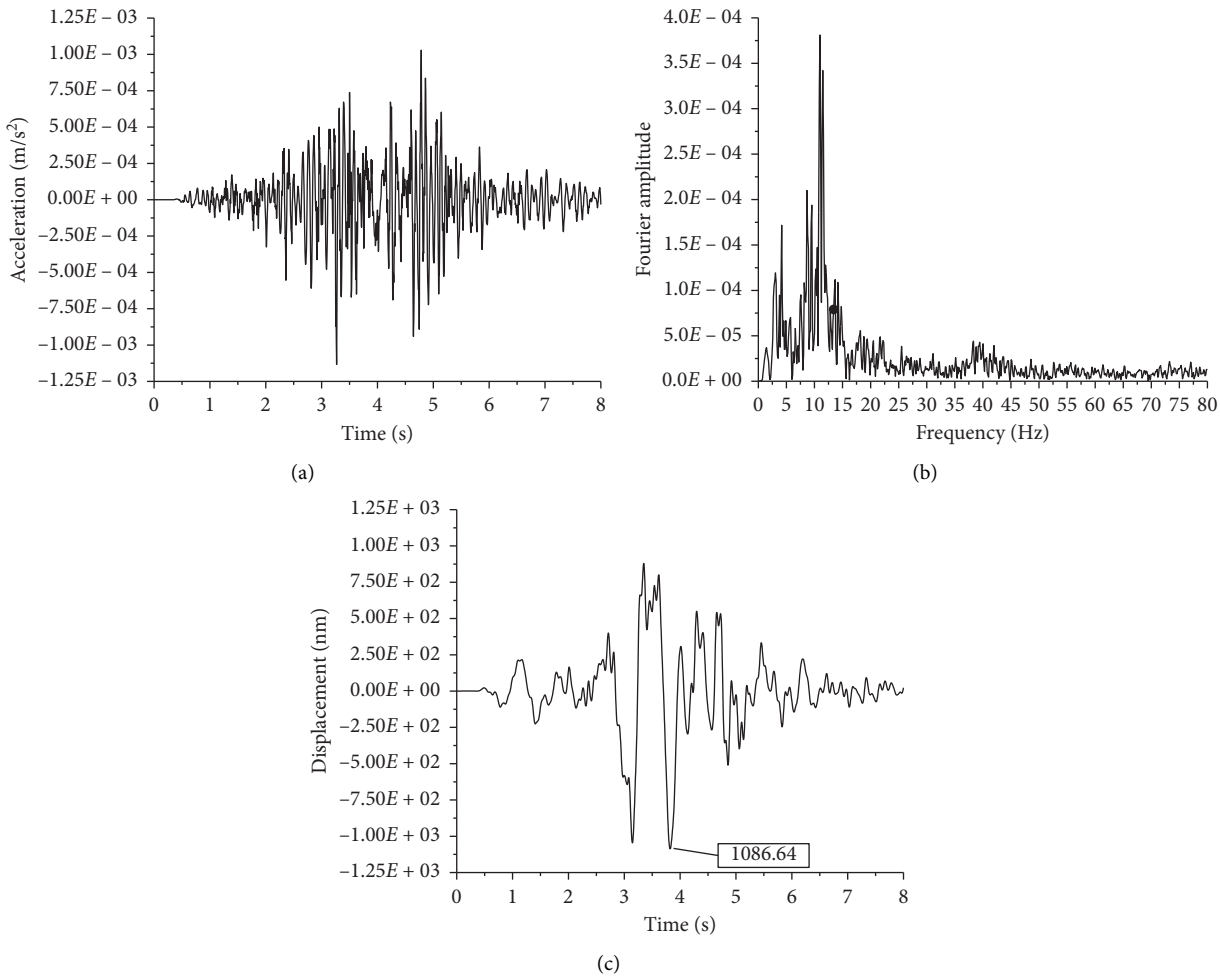

Figure 28: Numerical calculation results with no vibration-isolation measures: (a) acceleration time history, (b) frequency spectrum, and (c) displacement time history.

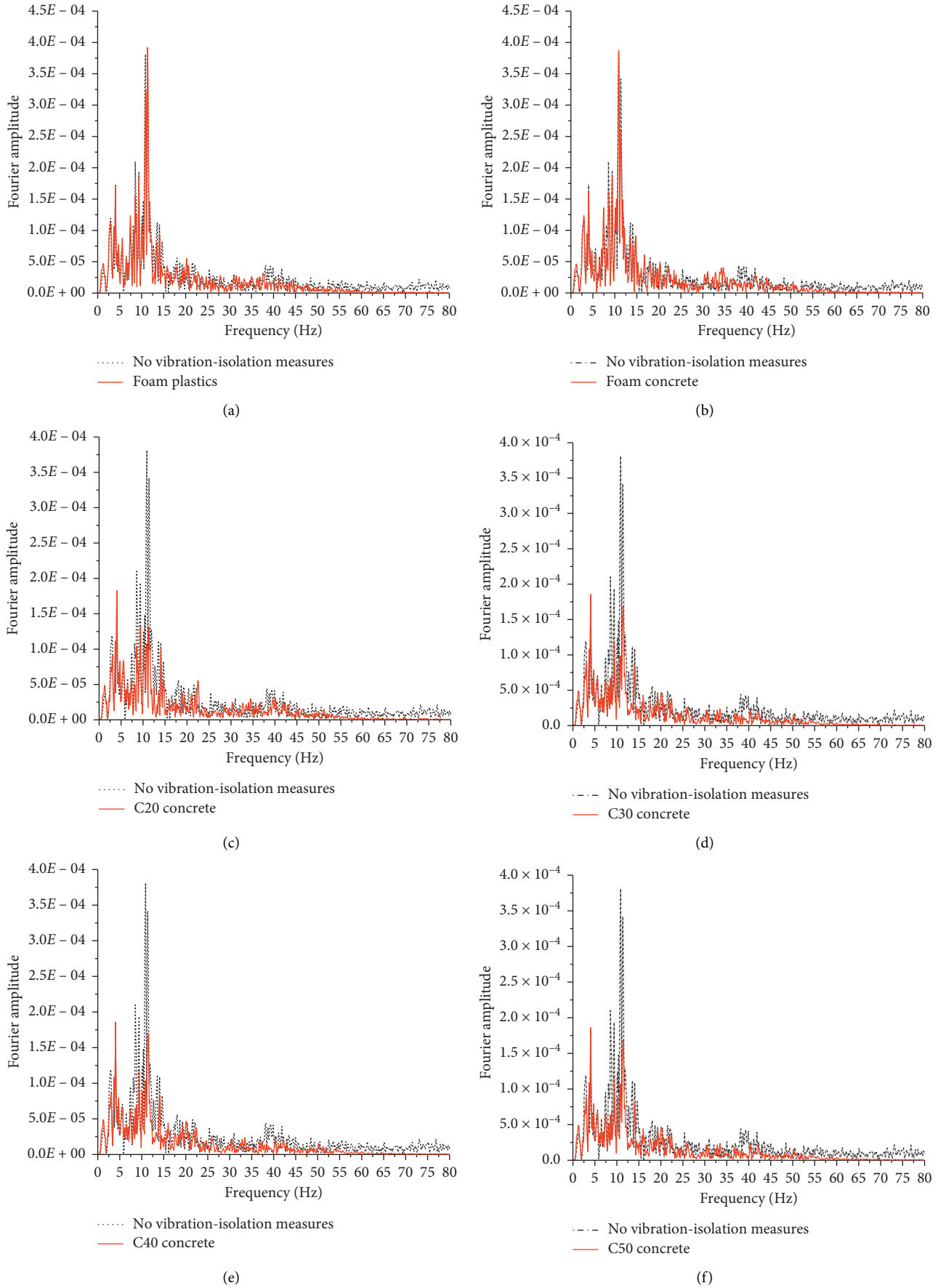

Figure 29: Influence of pile material on vibration-isolation effect (comparison of frequency spectra).

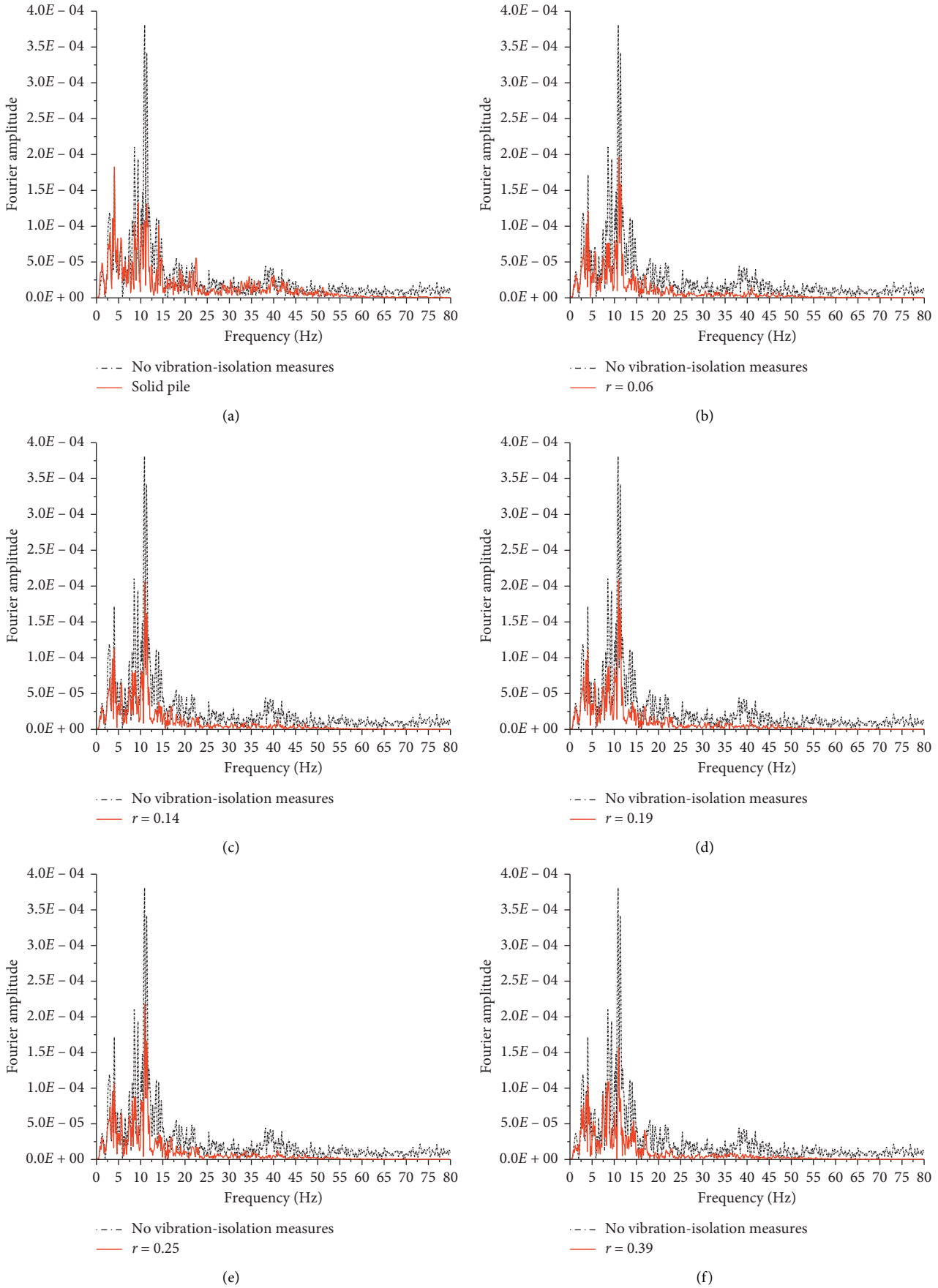

Figure 30: Influence of hollow ratio (r) on vibration-isolation effect (comparison of frequency spectra).

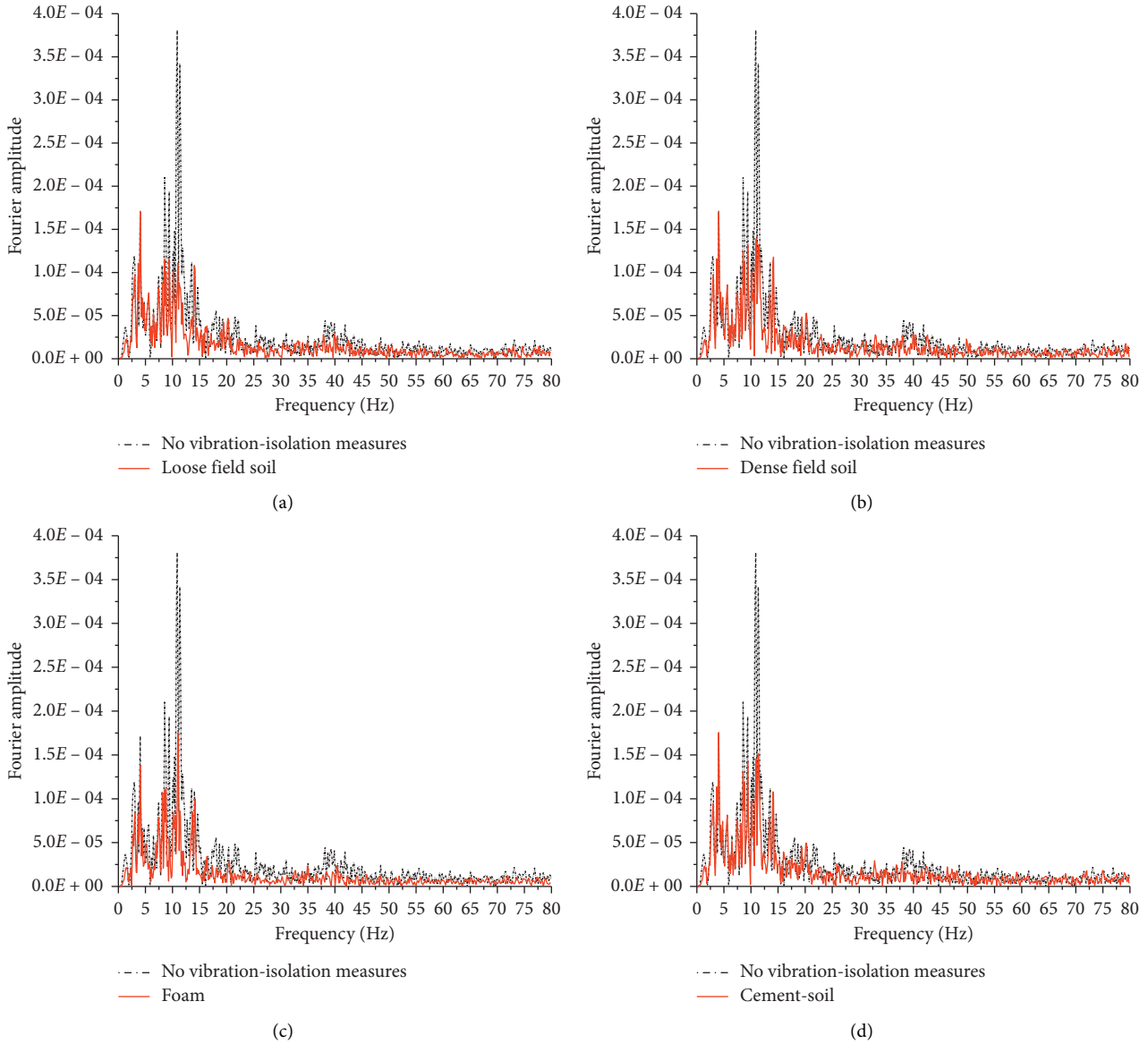

Figure 31: Influence of filling material on vibration-isolation effect (comparison of frequency spectra).

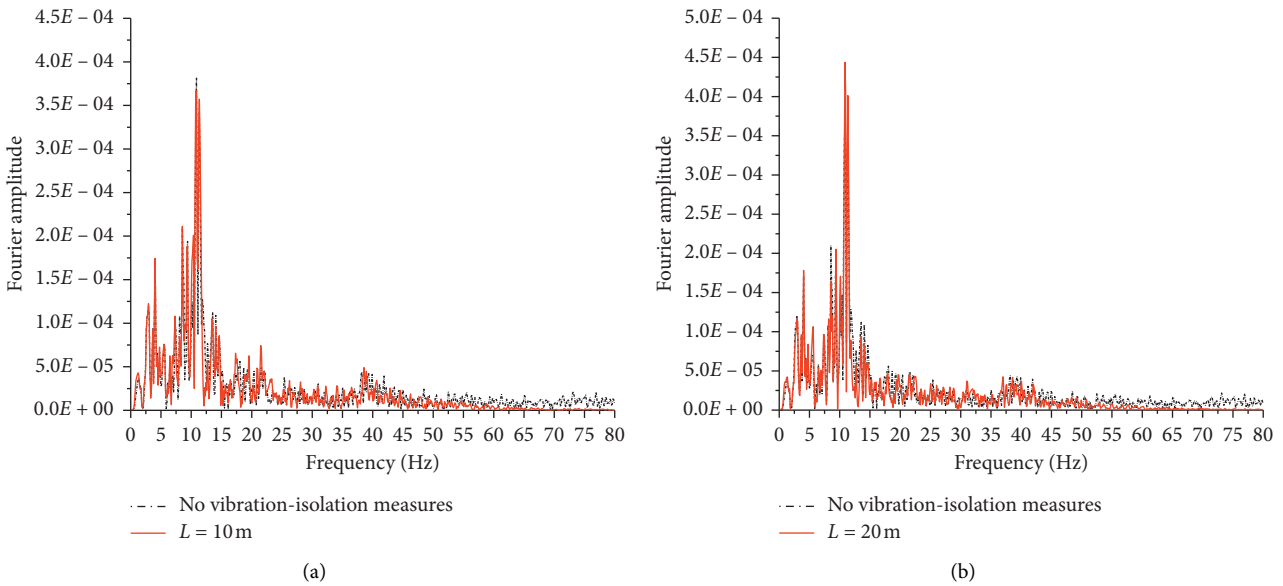

Figure 32: Continued.

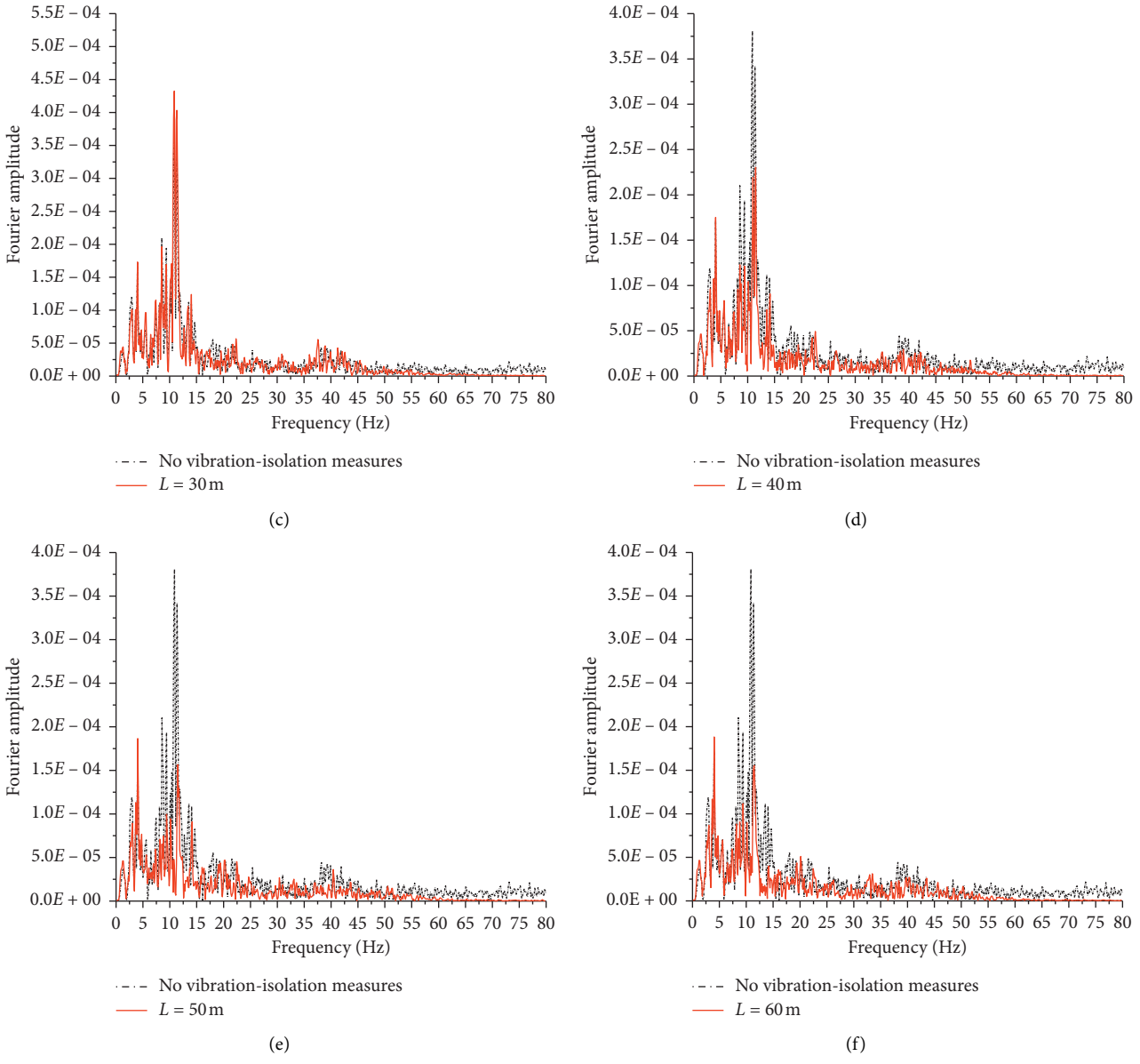

Figure 32: Influence of pile length (L) on vibration-isolation effect (comparison of frequency spectra).

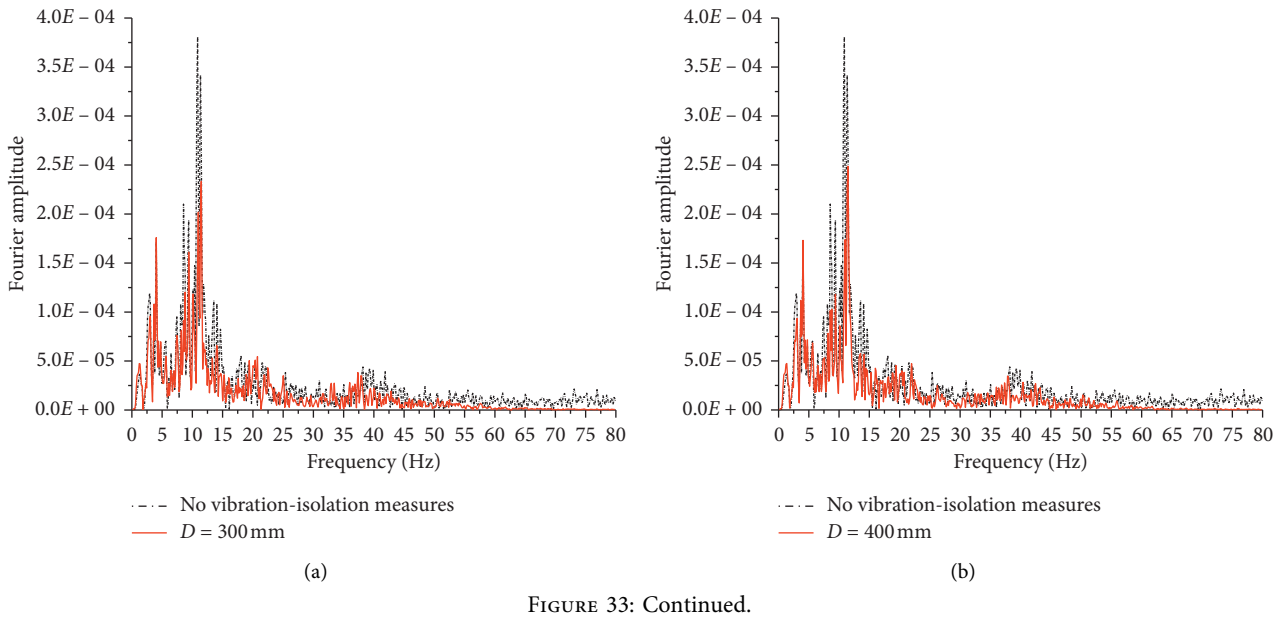

Figure 33: Continued.

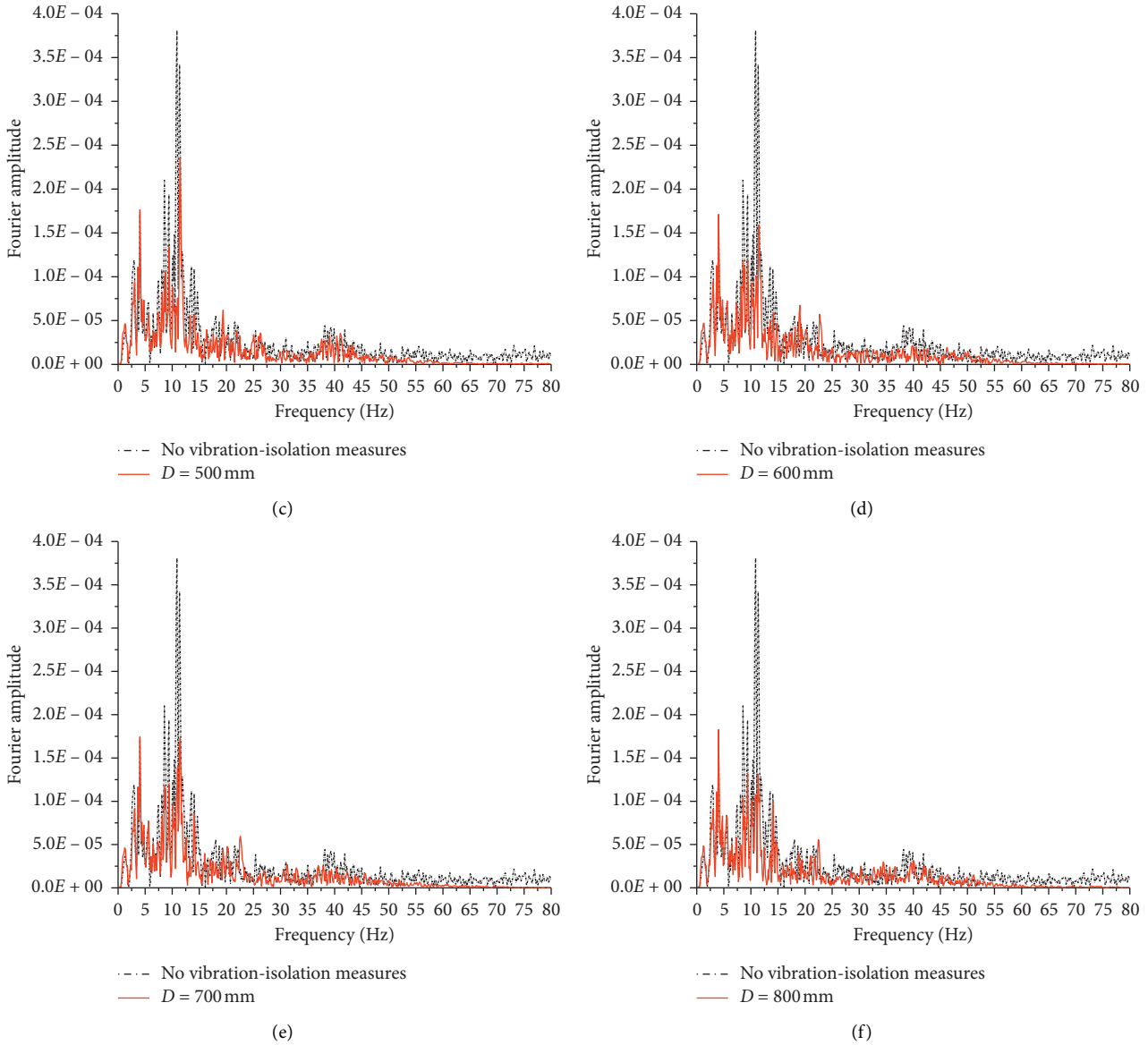

Figure 33: Influence of pile diameter (D) on vibration-isolation effect (comparison of frequency spectra).

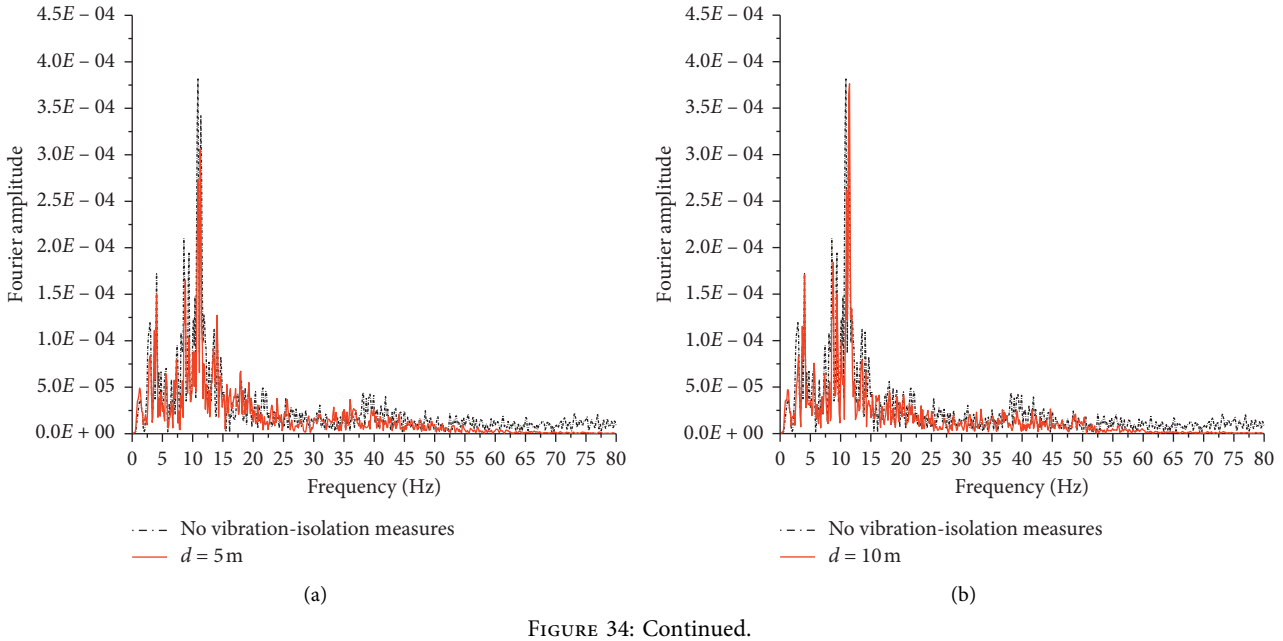

Figure 34: Continued.

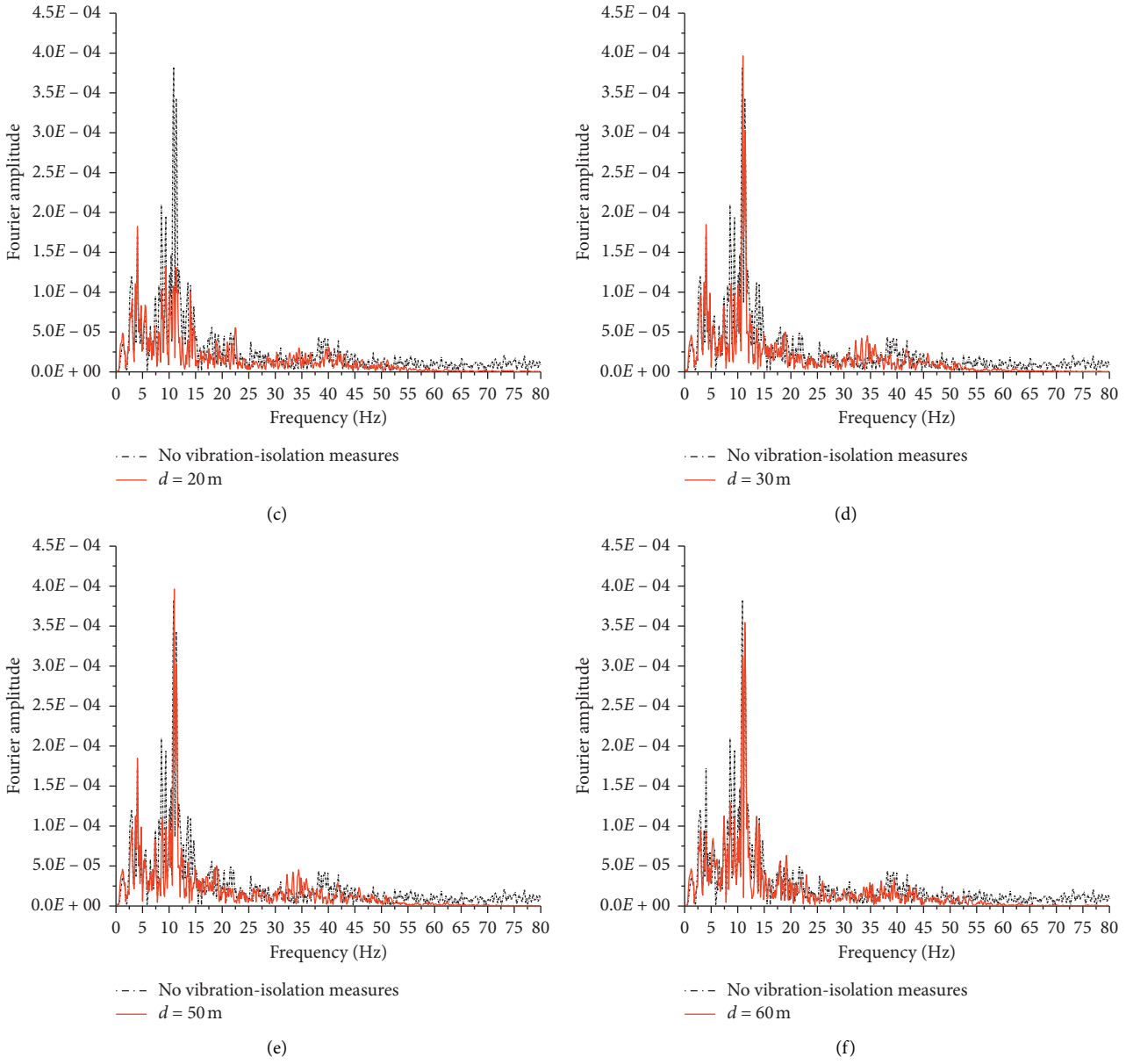

Figure 34: Influence of distance from hard-X-ray tunnel (d) on vibration-isolation effect (comparison of frequency spectra).

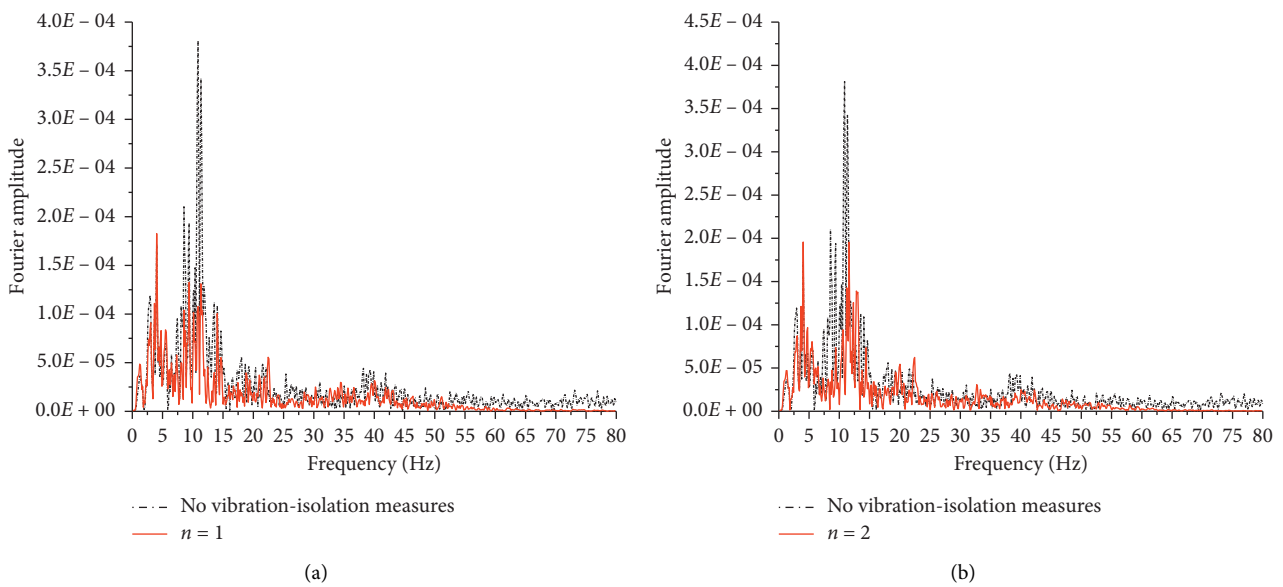

Figure 35: Continued.

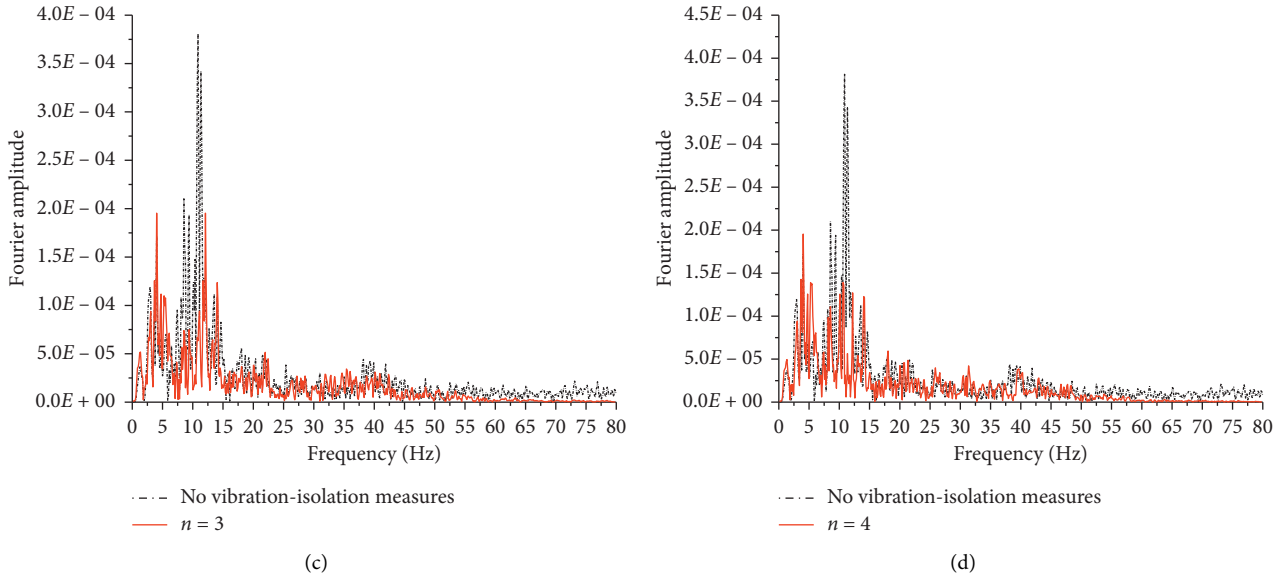

Figure 35: Influence of pile row number (n) on vibration-isolation effect (comparison of frequency spectra).

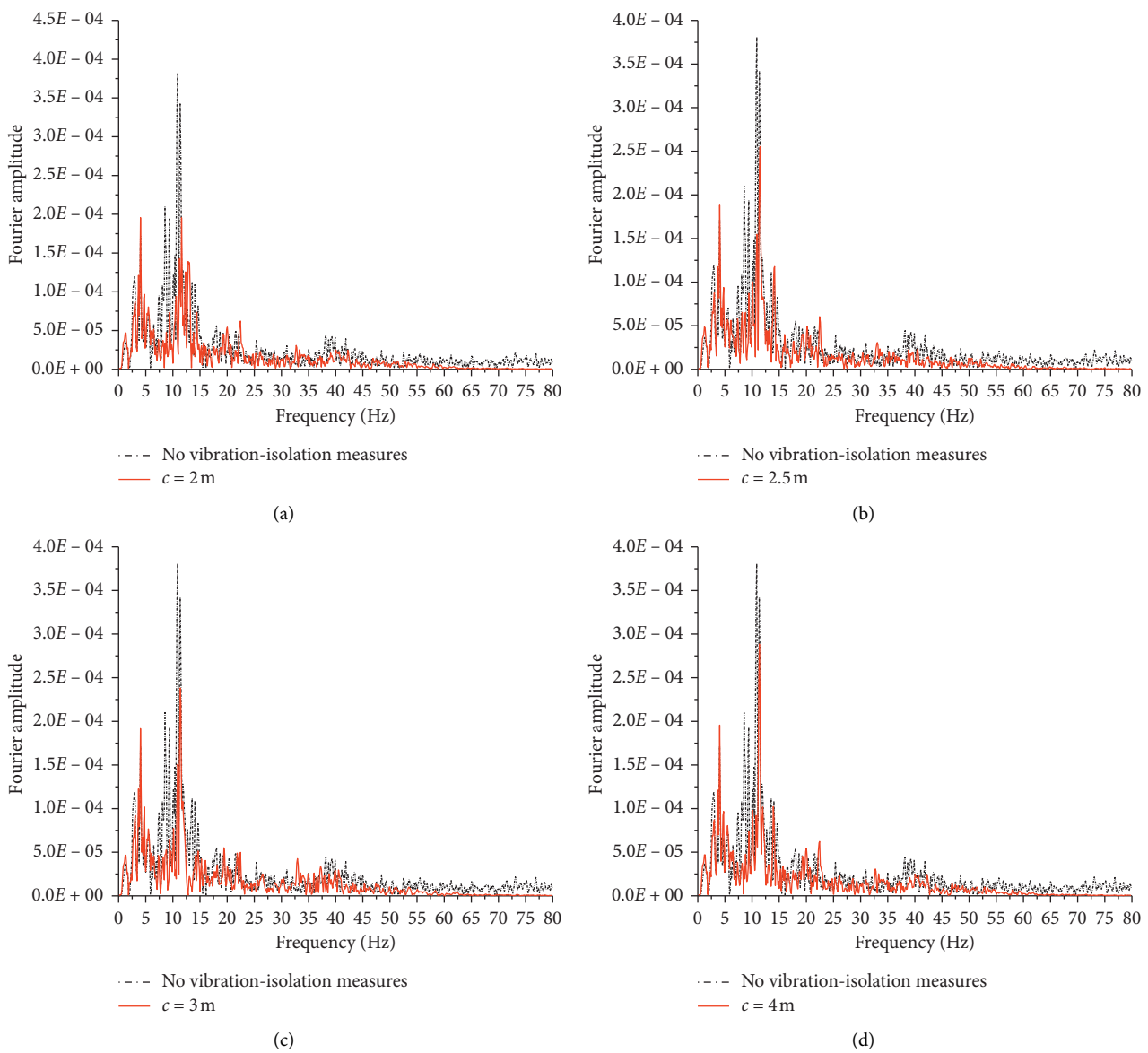

Figure 36: Continued.

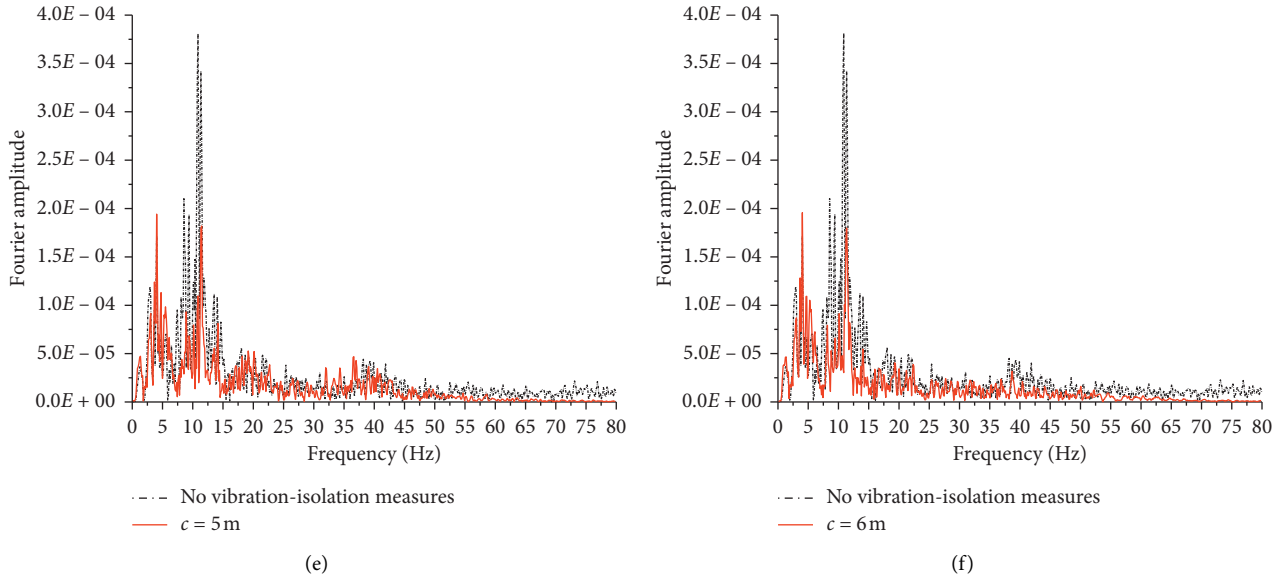

Figure 36: Influence of row spacing (c) on vibration-isolation effect (comparison of frequency spectra).

5. Conclusions

Based on a hard-X-ray tunnel under construction in Shanghai, relevant research was conducted on the vibration-isolation performance of a pile barrier in an area of soft soil. The main conclusions are as follows.

The vibration waves generated by the maglev, metro line 16 (viaduct part), and Luoshan Road viaduct traffic are concentrated mainly at middle and high frequencies, while those generated by the Luoshan Road ground traffic are concentrated mainly at low frequency. With increasing propagation distance and depth, the acceleration amplitude of the vibration waves is attenuated gradually. The high-frequency part of the vibration waves is attenuated rapidly in the soil, while the low-frequency part is attenuated slowly.

The attenuation law of the vibration waves in the soil as calculated by the numerical method is consistent with the field vibration measurements, thereby verifying the effectiveness of the numerical method in simulating environmental vibrations.

The pile body material, pile length, hollow ratio, filling material, and vibration-isolation position are the main factors affecting the vibration-isolation effect of the pile barrier. The vibration-isolation capacity of the pile barrier is proportional to the pile length, elastic modulus, and hollow ratio, and it is inversely proportional to the stiffness of the filling material. The pile diameter, row number, and row spacing have little influence on the vibration-isolation effect of the row piles. Increasing the pile diameter attenuates the acceleration amplitude around 10 Hz to a certain extent but basically has no influence on the acceleration amplitude around 5 Hz. With decreasing row spacing and increasing pile row number, the vibration-isolation effect of the row piles is improved slightly.

Data Availability

The data used to support the findings of this study are available from the corresponding author upon request.

Conflicts of Interest

The authors declare that they have no conflicts of interest.

Acknowledgments

This study was supported by the Shanghai Municipal Science and Technology Major Project (grant nos. 2017SHZDZX02and 17DZ1203902).

References

[1] S. Pennig, J. Quehl, U. Mueller et al., "Annoyance and self-reported sleep disturbance due to night-time railway noise examined in the field," *The Journal of the Acoustical Society of America*, vol. 132, no. 5, pp. 3109–3117, 2012.

[2] M. G. Smith, I. Croy, M. Ogren, and K. P. Waye, "On the influence of freight trains on humans: a laboratory investigation of the impact of nocturnal low frequency vibration and noise on sleep and heart rate," *PLoS One*, vol. 8, no. 2, Article ID e55829, 2013.

[3] M. Crispino and M. D'Apuzzo, "Measurement and prediction of traffic-induced vibrations in a heritage building," *Journal of Sound and Vibration*, vol. 246, no. 2, pp. 319–335, 2001.

[4] H. Takemiya, "Field vibration mitigation by honeycomb WIB for pile foundations of a high-speed train viaduct," *Soil Dynamics and Earthquake Engineering*, vol. 24, no. 1, pp. 69–87, 2004.

[5] S. Wolf, "Potential low frequency ground vibration (<6.3 Hz) impacts from underground LRT operations," *Journal of Sound and Vibration*, vol. 267, no. 3, pp. 651–661, 2003.

[6] J. T. Nelson, "Recent developments in ground-borne noise and vibration control," *Journal of Sound and Vibration*, vol. 193, no. 1, pp. 367–376, 1996.

[7] S. Gupta, W. F. Liu, G. Degrande et al., "Prediction of vibrations induced by underground railway traffic in Beijing," *Journal of Sound and Vibration*, vol. 310, no. 3, pp. 608–630, 2008.

[8] P. Chatterjee, G. Degrande, S. Jacobs et al., "Experimental results of free field and structural vibrations due to underground railway traffic," in *Proceedings of the 10th International Congress on Sound and Vibration*, pp. 387–394, Stockholm, Sweden, 2003.

[9] V. Aiello, D. Boiero, M. D'Apuzzo, L. V. Socco, and F. Silvestri, "Experimental and numerical analysis of vibrations induced by underground trains in an urban environment," *Structural Control and Health Monitoring*, vol. 15, no. 3, pp. 315–348, 2008.

[10] O. von Estorff and M. Adam, "Reduction of train-induced building vibrations by using open and filled trenches," *Computers & Structures*, vol. 83, no. 1, pp. 11–24, 2005.

[11] M. Sanayei, P. Maurya, and J. A. Moore, "Measurement of building foundation and ground-borne vibrations due to surface trains and subways," *Engineering Structures*, vol. 53, pp. 102–111, 2013.

[12] G. Gao, N. Li, and X. Gu, "Field experiment and numerical study on active vibration isolation by horizontal blocks in layered ground under vertical loading," *Soil Dynamics and Earthquake Engineering*, vol. 69, pp. 251–261, 2015.

[13] G. Gao, J. Chen, X. Gu, J. Song, S. Li, and N. Li, "Numerical study on the active vibration isolation by wave impeding block in saturated soils under vertical loading," *Soil Dynamics and Earthquake Engineering*, vol. 93, pp. 99–112, 2017.

[14] M. Gao, S. P. Tian, Y. Wang et al., "Isolation of ground vibration induced by high speed railway by DXWIB: field investigation," *Soil Dynamics & Earthquake Engineering*, vol. 131, Article ID 106039, 2020.

[15] M. Gao, X. Xu, Q. S. Chen et al., "Reduction of metro vibrations by honeycomb columns under the ballast: field experiments," *Soil Dynamics & Earthquake Engineering*, vol. 129, Article ID 105913, 2020.

[16] S. J. Chen, X. Z. Ling, Z. Y. Zhu et al., "Field monitoring on train-induced vibration in the seasonally frozen region of daqing in spring," in *Proceedings of the International Conference on Transportation Engineering*, Chengdu, China, 2012.

[17] D. Wei, W. X. Shi, R. L. Han et al., "Measurement and research on subway induced vibration in tunnels and buildings nearby in Shanghai," in *Proceedings of the International Conference on Multimedia Technology (ICMT)*, Hangzhou, China, July 2011.

[18] L. Schillemans, "Impact of sound and vibration of the North-South high-speed railway connection through the city of antwerp belgium," *Journal of Sound and Vibration*, vol. 267, no. 3, pp. 637–649, 2003.

[19] W. Gardien and H. G. Stuit, "Modelling of soil vibrations from railway tunnels," *Journal of Sound and Vibration*, vol. 267, no. 3, pp. 605–619, 2003.

[20] S. Liao and D. A. Sangrey, "Use of piles as isolation barriers," *Journal of Geotechnical and Geoenvironmental Engineering*, vol. 104, no. 9, pp. 1139–1152, 1978.

[21] Y. B. Yang, *Analysis on Soil Vibration Induced by High-Speed Railways*, Taiwan University, Taipei, Taiwan, 1996.

[22] H. Xia, *Vibration Engineering of Traffic Environment*, Science Press, Beijing, China, 2010.

[23] K. Ishihara, *Soil Behaviour in Earthquake Geotechnics*, Clarendon Press, Oxford, UK, 1996.

[24] X. Q. Gu, J. Yang, M. S. Huang et al., "Bender element tests in dry and saturated sand: signal interpretation and result comparison," *Soils and Foundations*, vol. 55, no. 5, pp. 952–963, 2015.

[25] B. M. Das and G. V. Ramana, *Principles of Soil Dynamics*, PWS-Kent Pub. Co., USA, 1993.

[26] J. B. Liu, Y. Gu, and Y. X. Du, "Consistent viscous-spring artificial boundary and Viscous-spring boundary element," *Chinese Journal of Geotechnical Engineering*, vol. 28, no. 9, pp. 1070–1075, 2006.

[27] Y. Gu, *Theoretical Analysis of the Efficient Numerical Method for Soil-Structure Dynamic Interaction and its Application*, Tsinghua University, Beijing, China, 2005.

[28] G. Y. Gao, Z. Y. Li, C. Qiu, and Z. Q. Yue, "Three-dimensional analysis of rows of piles as passive barriers for ground vibration isolation," *Soil Dynamics and Earthquake Engineering*, vol. 26, no. 11, pp. 1015–1027, 2006.

[29] G. Yue and Y. H. Li, "Three-dimensional analysis of a row of holes as active wave barrier in saturated soil," in *Proceedings of the GeoShanghai 2018 International Conference: Advances in Soil Dynamics and Foundation Engineering*, Shanghai, China, May 2018.